0.2 ml) was injected intraluminally. Images were obtained at the rate of 2.711 sec frame^{-1}. GFP-labeled structures were imaged by a 2PM customized for in vivo imaging (FV1000-MPE, Olympus, Tokyo) using a water-immersion objective lens (40X, NA0.8, Olympus) at zoom of 1.0. A Ti-sapphire laser (MaiTai Hp, Spectral Physics, Mountain View, CA, USA) was tuned to the excitation wavelength for GFP (950 nm). The z-stack images consisted of 100–300 optical sections and were taken 1 μm apart (within 400 μm of the serosal surface). The photomultiplier tube setting and excitation power (~50 mW) remained constant during imaging. Under these conditions, the neurons seem to be still healthy after imaging (personal communication from Dr. Go Kato).

Immunohistochemical Imaging by Confocal Microscope

Following in vivo imaging, the animals were euthanized by administration of excessive dose of Nembutal, and whole mount preparations of the anastomosed regions of ileum were fixed in 4% paraformaldehyde (4°C, overnight) or 99.5% acetone (4°C, 1 hr) to detect neurofilament (NF). Thereafter, the mucosa and submucosa and granulation tissue were carefully removed, and following a 30 min wash in PBS (0.01–0.1 mol L^{-1}, pH 7.4) the preparations were incubated for 3–12 hrs at 4°C in 10% normal donkey serum in PBS containing 0.3% (v/v) Triton-X 100 (PBS-TX) to enhance penetration of antibodies. The preparations were then incubated for two days at 4°C with a rabbit polyclonal antiserum cocktail to label NF (clone 2F11, reacting with 70, 160 and 200 kDa proteins, 0.5 μg/ml; DAKO). NF immunoreactivity was detected using an Alexa Fluor 594-conjugated secondary antibody (Invitrogen Inc., Carisbad, CA). Tissues were examined with an OLYMPUS FV1000 (Tokyo, Japan) confocal microscope. Confocal images were constructed as digital composites of Z-series scans of 10–15 optical sections through a depth of 10–20 μm or 100–150 μm. Final images were produced with the FV10-ASW software application [Ver1.7] (OLYMPUS).

Immunohistochemistry of Sectioned Preparations

The rectum including an anastomotic site was fixed with 4% paraformaldehyde at 4°C, and embedded in paraffin. Consecutive 4 μm sections were cut from each block. Immunostaining was performed by treatment with pepsin (DAKO Corp., Carpinteria, CA, USA) for 20 min at room temperature for NF, DLX2, GFP and GFAP. After endogenous peroxidase blockade with 3% H_2O_2-methanol for 15 min, specimens were rinsed with PBS and incubated with a primary antibody diluted with Washing Solution (BioGenex, San Ramon, CA, USA) at room temperature for 2 hours. The specimens were rinsed with PBS and incubated at room temperature for 1 hour with secondary antibody conjugated to peroxidase diluted at 0.5 μg mL^{-1} (Medical & Biotechnological Laboratories Co., Ltd., Nagoya, Japan). The sections were then rinsed with PBS and color-developed by diaminobenzidine (DAB) solution (DAKO) and counterstained with Meyer's hematoxylin (Sigma Chemical Co., St. Louis, MO, USA). Antibodies used in primary reaction and the working concentrations were as followed: anti-NF (clone 2F11, reacting with 70, 160, and 200 kDa proteins, 0.5 μg mL^{-1}, DAKO), anti-distal less homeobox 2 (DLX2)(cat. ab18188, 0.5 μg mL^{-1}, Abcam Co, Tokyo, Japan) as an enteric neural stem cell marker, anti-green fluorescent protein (GFP)(0.5 μg mL^{-1}, Rockland Immunochemicals Inc., Gilbertsville, PA) and glial fibrillary acidic protein (GFAP)(0.5 μg mL^{-1}, DAKO Corp, Carpintaria, CA) as an enteric glia cell marker.

Detection of Regenerated Enteric Neurons

To identify neuronal cell proliferation, 5-bromo-2-deoxyuridine, BrdU (1 mg mL^{-1} solution; Sigma or NACALAI TESQUE, INC, Kyoto, Japan) was added to the drinking water containing MOS (100 μM) for 1–2 weeks for 6 animals. After rinsing in PBS, the specimens were pretreated with sodium chloride sodium citrate solution for 2 hrs at 65°C, followed by partial denaturation of double-stranded DNA with 2 mol L^{-1} HCl for 30 min at 37°C. To reveal BrdU, the sections were incubated with a rat monoclonal antibody raised against BrdU (Abcam Inc.) overnight at 4°C. The specimens were rinsed in 0.1 mol L^{-1} TE (pH 7.8) followed by routine immunohistochemistry.

Statistics

Multiple comparisons were performed by one-way analysis of variance (ANOVA) with post-hoc Bonferroni's test. A value of $p<0.05$ was considered statistically significant. All data are expressed as the mean ± S.D.

Results

In the current study, we obtained the first in vivo images of enteric neurons and nerve fibers in the mucosa, submucosa,

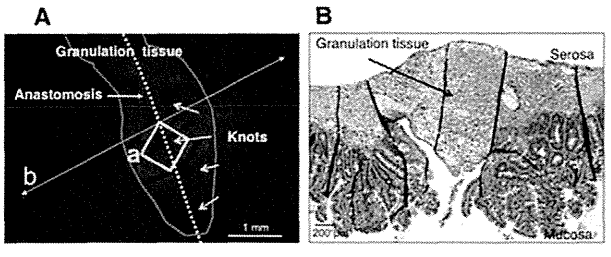

Figure 3. A stereomicroscopic image including the observed site shown in Figure 4. *A.* The thick granulation tissue at the anastomotic region in a mouse that was treated with MOS solution for 1 week after anastomosis surgery. An area in the square (**a**) corresponds to an area in the square (**a**) in **Figure 4**. *B.* A microscopic image of a longitudinal section, prepared following fixation, that was taken along the line (**b**) indicated in panel *A*.
doi:10.1371/journal.pone.0054814.g003

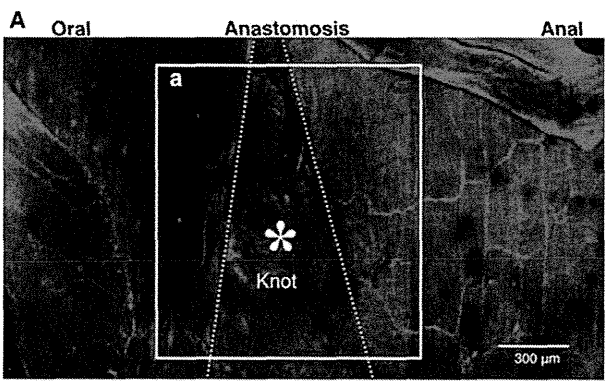

Figure 4. Immunohistochemical image for anti-neurofilament (NF) antibody of a whole mount preparation of the same intestine shown in Figure 5. *A–a* corresponds to Figure 5*A* (the image by 2PM). *, A knot of thread in the area between two-dotted lines indicates the anastomotic area. The granulation tissue was removed to allow for laser penetration. Normal myenteric plexus in the intact oral and anal sites are visible, but nerve cells and fibers are not visible in the anastomotic region because of the thickness of the anastomotic area.
doi:10.1371/journal.pone.0054814.g004

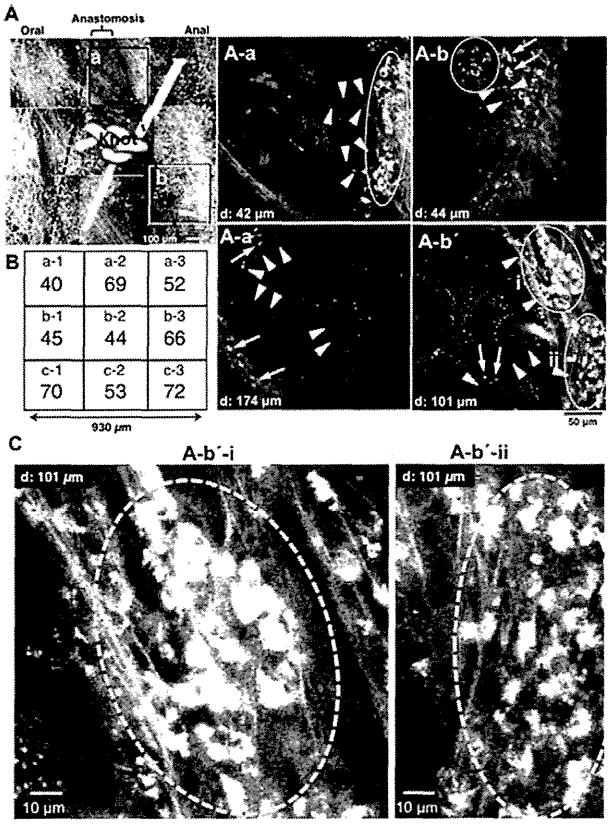

Figure 5. Images of anastomotic region of the terminal ileum in a MOS-treated mouse. The dotted lines indicates the anastomosis site. Around the knot of thread we obtained each image from 9 visual fields. ***A.*** Images stacked with Z axis to a total depth of 200–300 μm. ***A–a.*** image 42 μm deep to the serosa surface in area (***a***) in ***A. A–a´.*** image 174 μm deep to the serosa surface in the same area (***a***) in ***A. A–b.*** 44 μm deep to the serosa surface in area (***b***) in ***A. A–b´.*** image 101 μm deep to the serosa surface in the same area (***b***) in ***A.*** Arrows indicate nerve cells in ***A–a´, b*** and ***b´,*** and arrowheads indicate nerve fibers in ***A–a, a´, b*** and ***b´,*** and circles indicate ganglion-like clusters of neurons in ***A–a, b*** and ***b´,*** respectively. ***B.*** Number of neurons in each field (size: 310 μm×310 μm) around the knot. ***C.*** Newborn nerve cells formed ganglion structures indicated by circles. These were enlarged from the images shown in ***A–b´–i*** and ***–ii.***
doi:10.1371/journal.pone.0054814.g005

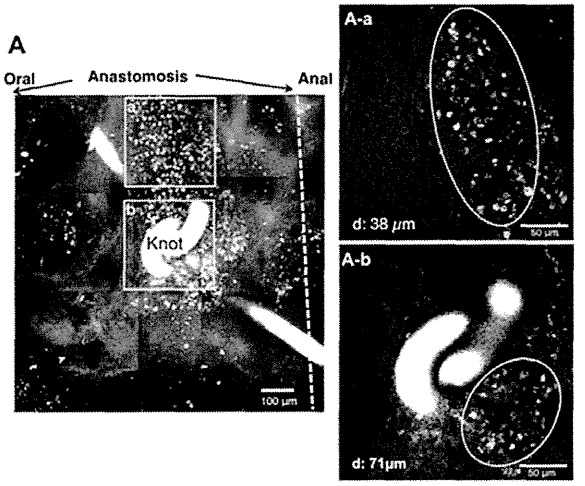

Figure 6. Images of anastomosis of the ileum in an SB-207266 (SB) plus MOS treated mouse. SB plus MOS treatment was performed for one week. ***A.*** Images stacked in the Z axis with a total depth of 200 - 300 μm. ***A–a.*** image 38 μm deep to the serosa surface in area (***a***) in ***A. A–b.*** image 71 μm deep to the serosa surface in area (***b***) in ***A.*** Circles indicate aggregates of small non-neuronal cells (***A–a*** and ***b***), respectively.
doi:10.1371/journal.pone.0054814.g006

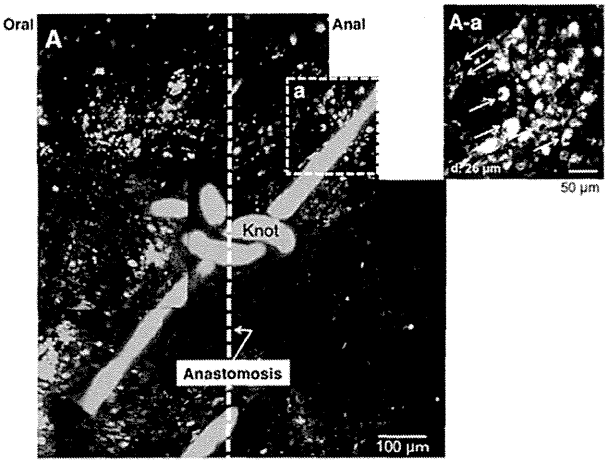

Figure 7. Images of around the suture knot at anastomosis of the ileum in DMSO treated mouse. Vehicle treatments were performed for 4 weeks. The dotted line indicates the anastomosis. ***A.*** Images stacked with Z axis up to a total depth of 151 - 201 μm. ***A–a.*** image 26 μm deep to the serosa surface close to the thread around the knot. A small number of neurons are visible.
doi:10.1371/journal.pone.0054814.g007

submucosal and myenteric plexuses, and circular and longitudinal muscles of the terminal ileum (**Figure 2**). We initially confirmed that enteric neurons could be imaged in vivo in the terminal ileum of an intact Thy1-GFP mouse (**Figure 2**). The normal mouse gut was rather thin, with a maximal thickness at myenteric ganglion level of 50 μm. Although images stacked with a Z-axis depth up to 50 μm showed low signal/background fluorescence intensity ratio, each image at depth of 28 μm–42 μm from serosa showed a single myenteric ganglion and longitudinal & circular muscle layers (**Figure 2*A–C***). Thicker images at depth of 60, 125 and 145 μm also showed nerve fibers in circular muscle layers, blood vessels and nerve fibers around crypts (Figure 2D–F), respectively. Living cells in a given ganglion were clearly observed in merged images at depth of 28 μm–50 μm (**Figure 2*G***).

A stereomicroscopic image demonstrating the thick granulation tissue at the anastomotic region in mouse treated with MOS solution for 1 week after surgical anastomosis is shown in **Figure 3*A***. However, under a stereomicroscopy no nerve cells or fibers were visible. A longitudinal section including the same granulation tissue indicates an obvious thickness of the tissue (**Figure 3*B***).

Using confocal imaging of the fixed whole mount preparation, no nerve cells or fibers were visible in the granulation tissue at the anastomosis, although intact myenteric plexus was visible in the intact area in a mouse treated with MOS solution for 1 week after surgery (**Figure 4**). The living ileum before fixation is shown in Figure 5.

In mice treated with MOS solution for 1 week after anastomosis, new ganglia-like structures and nerve fibers were

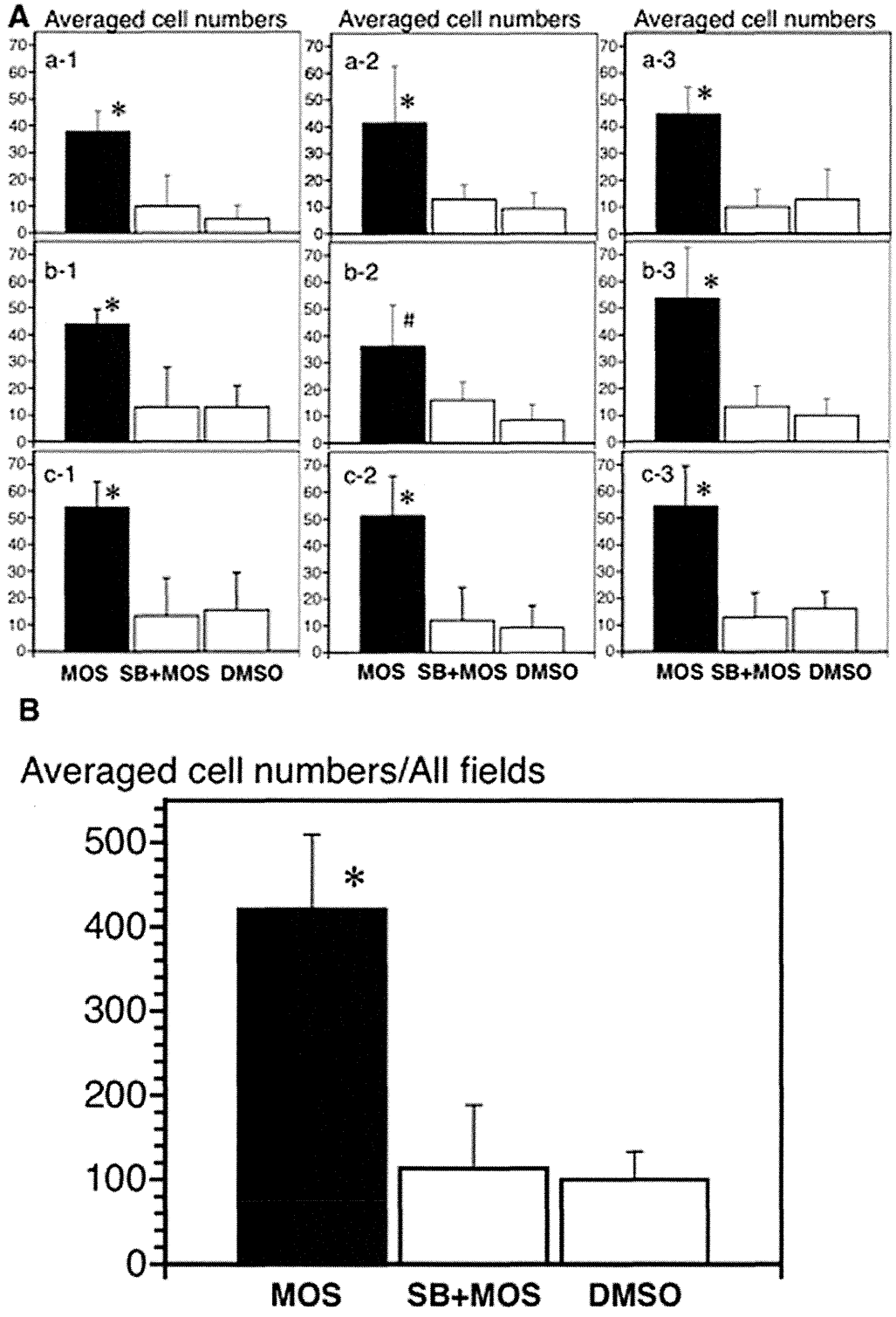

Figure 8. The average cell numbers in each of nine fields (A) and all fields (B) at the anastomosis. The comparison was performed among MOS (n = 5), SB+MOS (n = 4) and vehicle-treated (n = 4) mice. Each of the nine fields corresponds to that in Figure 5B. *, P<0.05 vs. SB+MOS and vehicle. #, P<0.05 vs. vehicle.
doi:10.1371/journal.pone.0054814.g008

observed by *in vivo* imaging of the thick granulation tissue at the anastomotic region of the living ileum (**Figure 5*A***). In sites both oral (**Figure 5*A–a* & *-a'***) and anal (**Figure 5*A–b* & *−b'***) to the anastomotic site, new ganglia-like structures packed with many of

newborn neurons and interganglionic nerve fibers were apparent in each image regardless of the depth from the serosa indicating that in the granulation tissue a new enteric neural network was being formed. The density of neurons observed within the anastomosis was 511 cells per 864,900 μm^2. The distribution of neurons was even in each nine field (from a−1 to c−3) (**Figure *5B***). **Figure 5*C*** clearly illustrates new neurons in two typical ganglion-like structures.

In mice treated with the 5-HT_4 antagonist, SB 207266 (SB) plus MOS solution for 1 week after anastomosis, no neurons or nerve fibers were observed in the anastomotic region (**Figure 6**), although aggregates of small cells (not neurons) were observed near the surface (**Figure 6*A–a* & *–b***). Thus, enteric neurogenesis was largely suppressed by simultaneous administration of the 5-HT_4 receptor blocker, SB along with MOS. Similar results were obtained with all 4 mice treated with MOS and SB.

Using confocal imaging of fixed, whole mount preparations, no nerve cells or fibers were visible in the granulation tissue at the anastomosis, although intact myenteric plexus was visible in the intact area in a mouse treated with SB and MOS solution for 1 week after surgery (data not shown).

Vehicle treated mice underwent in vivo imaging of the anastomotic region at 1 week (n = 5) and 4 weeks (n = 4) after ileum transection and re-anastomosis (**Figure 7**). One week after surgery, neither nerve bundles nor ganglia were visualized at the anastomosis. In contrast, 4 weeks after surgery, a small number of neurons were detected in one preparation (**Figure 7*A–a***). In the other three mice treated with vehicle for 4 weeks after surgery, no neurons were detected at any depth within the granulation tissue.

The average number of neurons observed amongst nine fields within the anastomosis in mice treated with MOS solution was significantly ($P<0.05$) larger than that in SB plus MOS treated mice (n = 4) or DMSO-treated mice (n = 4) after anastomosis (**Figure 8*A***). New neurons were observed without oral or anal and mesenteric or anti-mesenteric localizations in any of the three groups (**Figure 8*A***).

The average density of neurons observed in all fields within the anastomosis in mice treated with MOS solution was 421±89 per 864,900 μm^2 (n = 5), significantly ($P<0.05$) higher than SB plus MOS treated mice (113±76 per 864,900 μm^2; n = 4) or mice treated with vehicle (100±34 per 864,900 μm^2; n = 4) (Figure 8B). Moreover, the average number of neurons distributed at the anastomosis in MOS treated mice was about 5 cells per 10,000 μm^2, compared to 35 cells per 10,000 μm^2 (ganglia areas) in the intact small intestine of mice [11].

The distribution of neurons in depth was analyzed at depths of every 20 μm. In all three groups almost all neurons were located within 100 μm of the surface (**Figure 9*A–C***). The total number of neurons in MOS-treated mice was about four-fold of that in SB plus MOS and DMSO treated mice (**Figure 9*D***).

Correctly identified fluorescent neurons by 2PM are proved to be neurons with an independent technique at the anastomotic site. NF-positive, DLX2-negative, BrdU-positive and GFP-positive cell is identified as a new neuron (**Figure 10*A–D***). NF-negative, DLX2-positive, BrdU-positive and GFP-positive cells seem to be neural progenitors. At this anastomotic site, GFAP-positive enteric glial cells are not found (**Figure 10*E***).

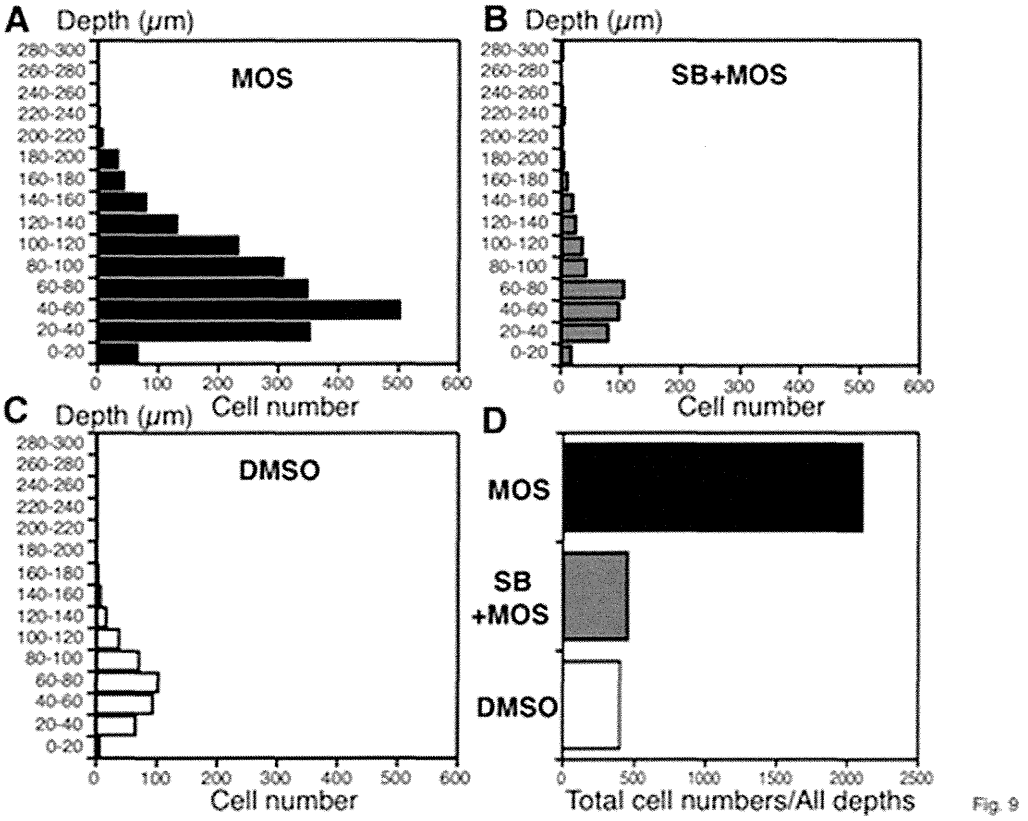

Figure 9. The distribution of total neurons in MOS (n = 5), SB+MOS (n = 4) and vehicle-treated (n = 4) mice. *A, B, C.* Number of total neurons at depths of every 20 μm. *D.* Cumulative numbers from all depths.
doi:10.1371/journal.pone.0054814.g009

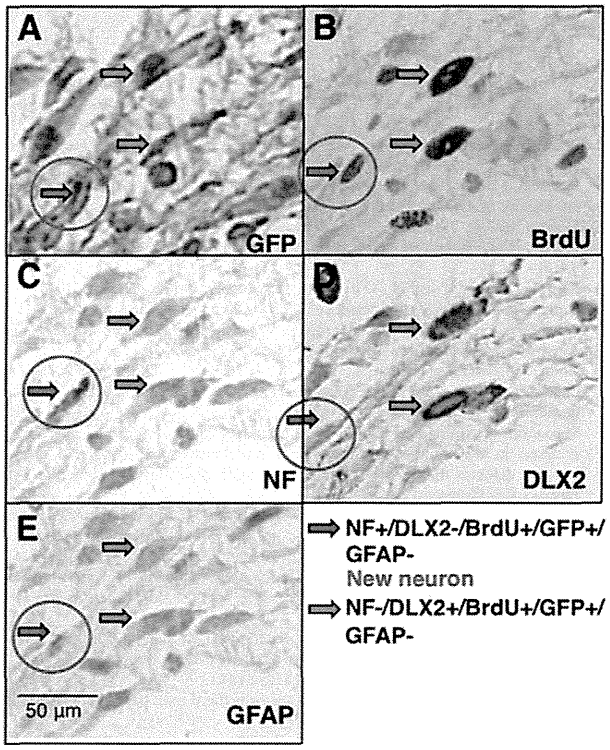

Figure 10. Correctly identified fluorescent neurons by 2PM are proved to be neurons at the anastomosis in MOS-treated mice. *A.* Green Fluorescent Protein (GFP)-positive cells. *B.* 5-bromo-2′-deoxyuridine (BrdU)-positive cells. *C.* A neural marker, neurofilament (NF)-positive cell. *D.* A neural stem cell marker, distal less homeobox 2 (DLX2)-positive cells. *E.* glial fibrillary acidic protein (GFAP)-negative cells. Red arrows indicate NF+/DLX2−/BrdU+/GFP+/GFAP- cell: this cell is a new neuron. Green arrows indicate NF−/DLX2+/BrdU+/GFP+/GFAP- cells: these cells seem to be neural progenitors. Similar results are obtained in other preparations.
doi:10.1371/journal.pone.0054814.g010

Discussion

This is the first study involving in vivo imaging of enteric neurons with 2PM, although in vivo imaging of enteric neurons with confocal laser endomicroscopy has been recently performed [9]. We detected the formation of newly generated neurons in the thick granulation tissue at the site of anastomosis. Imaging with 2 PM allowed enteric neural imaging several hundred microns deep within the gut of living mouse. In contrast to the brain tissue [7], the structure of the gut tissue is complex, consisting of multiple layers and tissue types, including mucosa, submucosa, circular and longitudinal muscles, blood vessels and crypt glands. Therefore, to enhance visualization of enteric neurons we used Thy1-GFP mice [8] after confirmation of expression of cytoplasmic GFP in enteric neurons in preliminary studies. In the present study, newly formed enteric neurons also expressed cytoplasmic GFP. In future studies, we are planning functional studies of enteric neurons using in vivo imaging with 2PM and genetically encoding calcium indicators [12].

A critical obstacle to overcome in order to obtain clear images of enteric neurons in vivo was to suppress motion disturbance associated with gut motility. Otherwise, observed images would be blurry and non-interpretable. We found that pinning and intraluminal injection of papaverine eliminated tissue movement and allowed for the acquisition of sharp images.

One week after surgical anastomosis, MOS facilitated formation of newly generated enteric neurons in the granulation tissue at the anastomosis. However, even 4 weeks after surgery, only a small number of newborn neurons were identified in the granulation tissue of vehicle-treated control animals. The effects of MOS on neurogenesis were completely antagonized by treatment with a 5-HT_4 receptor antagonist, indicating that MOS facilitated formation of newborn enteric neurons via 5-HT_4-receptor activation. Although the number of newly formed enteric neurons was significantly higher in the MOS-treated mice as compared to antagonist treated and vehicle controls, the distribution pattern of newly formed enteric neurons was similar, i.e., neurons were distributed close to the edge of the granulation tissue. This suggested the possibility that neural stem cells were mobilized from the outside of the granulation tissue.

Enteric nervous system (ENS) development is relevant to Hirschsprung's disease (HSCR; congenital aganglionosis of the terminal bowel) and related diseases, which are still imperfectly treated. It is well known that mutations in genes encoding the Ret receptor tyrosine kinase and endothelin receptor type B are involved in HSCR pathogenesis [13,14]. We found MOS increased mRNA of c-Ret receptor tyrosine kinase in a rat model and that a 5-HT_4 receptor antagonist completely blocked this effect [15]. Therefore, it seems likely that the target molecule of MOS is the Ret receptor tyrosine kinase.

Enteric neurogenesis must be strictly controlled, because hyperplasia of enteric neurons due to hypersensitivity for glial cell-derived neurotrophic factor (GDNF)-Ret signaling reversely results in HSCR [16]. Nevertheless, treatment with 5-HT_4 receptor agonists such as MOS could be a promising tool to treat HSCR and related disorders.

In conclusion, *in vivo* imaging by 2PM allowed for high-resolution deep imaging of the intestines *in vivo*. Thick granulation tissue at the site of anastomosis, including newly formed ganglion-like structures and nerve fibers, could be studied in the intact murine small intestine, whereas this would have been impossible with traditional fluorescence or confocal microscopy. The results presented here confirmed that oral administration of MOS promotes the generation of enteric neurons by activation of enteric neural 5-HT_4-receptors in the murine small intestine. The present technology would be promising for *in vivo* imaging of enteric neurons distributed throughout the entire gastrointestinal tract as a means of evaluating enteric neural function and dysfunction in the normal gut and in, for example, diabetic [17] and parkinsonism mouse models [18].

The recent publications suggest that mouse enteric glia can be neuronal precursors and thus form neurons *in vitro* and *in vivo* under specific circumstances [19–21]. Therefore, we have investigated glia and/or their relation to the newly formed "neurons". However, we did not found any enteric glial cells at the anastomotic site. It seems unlikely that enteric glial cells contribute to neurogenesis at least at the anastomotic site.

Acknowledgments

We thank Prof. Gary Mawe in the Department of Anatomy and Neurobiology in the University of Vermont for his critical reading of this manuscript.

Author Contributions

Conceived and designed the experiments: KG HK JN MT. Performed the experiments: KG GK YL HM TI. Analyzed the data: KG GK HK JN MT. Contributed reagents/materials/analysis tools: KG IK YL KO. Wrote the paper: KG MT.

References

1. Katsui R, Kojima Y, Kuniyasu H, Shimizu J, Koyama F, et al. (2008) A new possibility for repairing the anal dysfunction by promoting regeneration of the reflex pathways in the enteric nervous system. Am J Physiol Gastrointest Liver Physiol 294: G1084–G1093.
2. Yamanouchi M, Shimatani H, Kadowaki M, Yoneda S, Nakagawa T, et al. (2002) Integrative control of rectoanal reflex in guinea pigs through lumbar colonic nerves. Am J Physiol Gastrointest Liver Physiol 283: G148–G156.
3. Matsuyoshi H, Kuniyasu H, Okumura M, Misawa H, Katsui R, et al. (2010) A 5-HT_4-receptor activation-induced neural plasticity enhances in vivo reconstructs of enteric nerve circuit insult. Neurogastroenterol Motil 22: 806–e226.
4. Takaki M, Misawa H, Matsuyoshi H, Kawahara I, Goto K, et al. (2011) In vitro enhanced differentiation of neural networks in ES gut-like organ from mouse ES cells by a 5-HT_4-receptor activation. Biochem Biophys Res Commun 406: 529–533.
5. Liu M, Gershon MD (2006) Neuroprotective/trophic effects of 5-HT_4 receptor stimulation on enteric neurons of mice. Neurogastroenterol Motil 18: 780–781.
6. Liu M-T, Kuan Y-H, Wang J, Hen R, Gershon MD (2009) 5-HT_4 Receptor-mediated neuroprotection and neurogenesis in the enteric nervous system of adult mice. J Neurosci 299: 683–969.
7. Wake H, Moorhouse AJ, Jinno S, Kohsaka S, Nabekura J (2009) Resting microglia directly monitor the functional state of synapses in vivo and determine the fate of ischemic terminals. J Neurosci 29: 3974–3980.
8. Feng G, Mellor RH, Bernstein M, Keller-Peck C, Nguyen QT, et al. (2000) Imaging neuronal subsets neurotechnique in transgenic mice expressing multiple spectral variants of GFP. Neuron 28: 41–51.
9. Ohya TR, Sumiyama K, Takahashi-Fujigasaki J, Dobashi A, Saito S, et al. (2012) In vivo histologic imaging of the muscularis propria and myenteric neurons with probe-based confocal laser endomicroscopy in porcine models (with videos). Gastroinrestinal Endoscopy 75: 405–410.
10. Bharucha AE, Camilleri M, Haydock S, Ferber I, Burton D, et al. (2000) Effects of a serotonin 5-HT_4 receptor antagonist SB-207266 on gastrointestinal motor and sensory function in humans. Gut 47: 667–674.
11. Thacker M, Rivera LR, Cho H-J, Furness JB (2011) The relationship between glial distortion and neuronal changes following intestinal ischemia and reperfusion. Neurogastroenterol Motil 23: e500–e509.
12. Nakai J, Ohkura M, Imoto K (2001) A high signal-to-noise Ca^{2+} probe composed of a single green fluorescent protein. Nature Biotechnol 19: 137–141.
13. Gershon MD (2010) Developmental determinants of the independence and complexity of the enteric nervous system. Trends in Neuroscience 33: 446–456.
14. Hofstra RMW, Osinga J, Buys CHCM (1997) Mutations in Hirschsprung disease: When does a mutation contribute to the phenotype. Eur J Hum Genet 5: 180–185.
15. Kawahara I, Kuniyasu H, Matsuyoshi H, Goto K, Obata K, et al. (2012) The comparison of effects of a selective 5-HT reuptake inhibitor versus a 5-HT_4 receptor agonist on in vivo neurogenesis at the rectal anastomosis in rats. Am J Physiol Gastrointest Liver Physiol 302: G588–G597.
16. Zhou R, Niwa S, Homma N, Takei Y, Hirokawa N (2009) KIF26A is an unconventional kinesin and regulates GDNF-Ret signaling in enteric neuronal development. Cell 139: 802–813.
17. Surendran S, Kondapaka SB (2005) Altered expression of neuronal nitric oxide synthase in the duodenum longitudinal muscle-myenteric plexus of obesity induced diabetes mouse: Implicatoins on enteric neurodegeneration. Biochem Biophys Res Commun 338: 919–922.
18. Kurosaki M, Muramatsu Y, Kato H, Araki T (2004) Biochemical, behavioral and immunohistochemical alterations in MTPT-treated mouse model of Parkinson's disease. Pharmacol Biochem Behavior 78: 143–153.
19. Joseph NM, He S, Quintana E, Kim Y-G, Núñez G, et al. (2011) Enteric glia are multipotent in culture but primarily form glia in the adult rodent gut. J Clin Invest 121: 3398–3411.
20. Laranjeira C, Sandgren K, Kessaris N, Richardson W, Potocnik A, et al. (2011) Glial cells in the mouse enteric nervous system can undergo neurogenesis in response to injury. J Clin Invest 121: 3412–3424.
21. Gershon MD (2011) Behind an enteric neuron there may lie a glial cell. J Clin Invest 121: 3386–3389.

FULL PAPER

BJC

British Journal of Cancer (2013) 108, 1460–1469 | doi: 10.1038/bjc.2013.27

Keywords: apoptosis; VEGF; integrin; MAPK

Protumoral roles of melanoma inhibitory activity 2 in oral squamous cell carcinoma

M Kurihara[1,2], T Kirita[2], T Sasahira[1], H Ohmori[1], S Matsushima[1], K Yamamoto[2], A K Bosserhoff[3] and H Kuniyasu[*,1]

[1]*Department of Molecular Pathology, Nara Medical University, 840 Shijo-cho, Kashihara, Nara 634-8521, Japan;* [2]*Department of Oral and Maxillofacial Surgery, Nara Medical University, Kashihara, Japan and* [3]*Department of Molecular Pathology, Institute of Pathology, University of Regensburg, Regensburg, Germany*

Background: The role of melanoma inhibitory activity 2 (MIA2) was examined in human oral squamous cell carcinoma (OSCC).

Methods: MIA2 role was examined by immunohistochemistry of human OSCCs and knockdown studies using human 3 OSCC cell lines with MIA2 expression.

Results: MIA2 expression was observed in 62 (66.7%) of 93 OSCCs and was associated with tumour expansion and nodal metastasis. Melanoma inhibitory activity 2 expression was inversely correlated with intratumoral infiltration of lymphocytes. Invasion and anti-apoptotic survival were reduced by MIA2 knockdown in HSC3 cells. MOLT-3 lymphocytes infiltrating the HSC3 cell layer was enhanced by MIA2 knockdown or MIA2 depletion with the antibody. In HSC3 cells, MIA2 knockdown decreased the expressions of vascular endothelial growth factor (VEGF), VEGF-C, and VEGF-D. The downregulation of VEGF-C and -D was caused by inhibition of p38 and extracellular signal-regulated kinase (ERK)1/2, respectively. Melanoma inhibitory activity 2 was co-precipitated with integrin α4 andα5 in HSC3 cells. Integrin α4 knockdown decreased p38 phosphorylation and increased apoptosis, whereas integrin α5 knockdown decreased c-Jun N-terminal kinase (JNK) phosphorylation and apoptosis. Inhibition of JNK decreased apoptosis in the HSC3 cells.

Conclusion: These findings suggest that the roles of MIA2 might be based on the variety of the integrins and the subtypes of mitogen-activated protein kinase.

Oral squamous cell carcinoma (OSCC) is the most common cancer resulting from the oral habits of smoking, reverse smoking, and betel nut chewing, accounting for at least 40% of cancer cases in South Asia, including India and Sri Lanka (Ferlay *et al*, 2010). In Japan, OSCC comprises ~1–2% of all cancer morbidity, a rate that is gradually increasing (Matsuda *et al*, 2012). Oral squamous cell carcinoma frequently leads to dysfunction of mastication, speech, and deglutition, which worsen a patient's quality of life. Moreover, the prognosis of OSCC remains poor: the overall 5-year survival rate has remained at ~56% over the past 2 decades (Nagler, 2002; Kademani *et al*, 2005). The poor prognosis of OSCC is associated with local invasion and lymph node metastasis (Lopez-Graniel *et al*, 2001).

Angiogenesis and lymphangiogenesis, pivotal events in tumour progression and metastasis (Adams and Alitalo, 2007; Avraamides *et al*, 2008), are responsible for local invasion and lymph node metastasis and a subsequently worse prognosis (Miyahara *et al*, 2007). Tumour cells have been reported to induce angiogenesis and lymphangiogenesis by expressing angiogenesis factor vascular endothelial growth factor (VEGF) and the lymphangiogenic factors VEGF-C and VEGF-D (Beck and D'Amore, 1997; Tsurusaki *et al*, 1999; Yonemura *et al*, 1999). In OSCC, like in other tumours, VEGF predominantly induces tumour angiogenesis, whereas VEGF-C and VEGF-D induce lymphangiogenesis (Shintani *et al*, 2004). A significant association between elevated VEGF circulating levels and clinical stage (Shang *et al*, 2002), and a possible relationship between the VEGF-C and/or VEGF-D expression levels and the development of lymphatic tumour spread were revealed in patients with OSCC (Shintani *et al*, 2004). We previously reported that melanoma inhibitory activity (MIA) is

*Correspondence: Dr H Kuniyasu; E-mail: cooninh@zb4.so-net.ne.jp

Received 10 October 2012; revised 2 January 2013; accepted 7 January 2013; published online 19 March 2013

closely involved in tumour progression and nodal metastasis by the increments of VEGF-C and VEGF-D in OSCC (Sasahira *et al*, 2010).

Melanoma inhibitory activity 2 (MIA2) belongs to the MIA gene family, which contains MIA, OTOR, and Tango (Bosserhoff and Buettner, 2002). Melanoma inhibitory activity 2 is mapped to the gene locus of human chromosome 14q13 (Bosserhoff *et al*, 2003b). Melanoma inhibitory activity and OTOR are exclusively expressed in the cartilage and cochlea, respectively, whereas MIA2 is expressed exclusively in the liver (Bosserhoff *et al*, 2003b). Melanoma inhibitory activity 2 expression is transcriptionally regulated by the hepatocyte nuclear factor (HNF)-1-binding site (Hellerbrand *et al*, 2005). Melanoma inhibitory activity 2 is expressed in hepatocellular carcinoma (HCC) but not in bladder, breast, or prostate cancer (Hellerbrand *et al*, 2005). Melanoma inhibitory activity 2 inhibits HCC growth and invasion, and consequently acts as a tumour suppressor (Hellerbrand *et al*, 2008). Hepatic MIA2 expression is increased in patients with liver fibrosis or cirrhosis and tumour growth factor-β (TGF-β)-induced MIA2 expression in hepatocytes (Bosserhoff *et al*, 2003a). It is well known that TGF-β signalling is deranged in HCC (Hellerbrand *et al*, 2008). Therefore, it may be speculated that TGF-β signalling contributes to the reduced MIA2 transcriptional activity observed in HCC. Loss of HNF-1 expression in HCC affects tumorigenicity by downregulating MIA2 (Hellerbrand *et al*, 2008). In OSCC, the expression and role of MIA2 have not been elucidated previously.

In this study, we investigated the relationship between MIA2 expression and clinicopathological characteristics to determine its functional role in OSCC.

MATERIAL AND METHODS

Patients and tumour specimens. Ninety-three formalin-fixed (43 men, 50 women) paraffin-embedded specimens of primary OSCC cases were randomly selected, which were operated at the Nara Medical University Hospital from 2002 to 2005. Medical records and prognostic follow-up data were obtained from the patient database administered by the hospital. The primary site of the cases was tongue (52 cases), gingiva (27 cases), buccal mucosa (9 cases), and other (5 case). The tumours were classified according to the International Union Against Cancer TNM classification system (Kreppel *et al*, 2010).

Immunohistochemistry. Consecutive 3-μm sections were cut from each block. Immunohistochemistry was performed by the immunoperoxidase technique, following antigen retrieval by incubation with pepsin (Sigma Chemical, St Louis, MO, USA) for 20 min, specimens were rinsed with phosphate-buffered saline (PBS, Sigma). Antibodies for MIA2 (Abcam, Cambridge, UK), CD3, CD4, CD8, CD20 (DAKO, Carpinteria, CA, USA), CD40L (AbD Serotec, Oxford, UK), granzyme B (Spring Bioscience, Pleasanton, CA, USA), and FOXP3 (Origene Technology, Rockville, MD, USA), diluted at 0.5 $\mu g\,ml^{-1}$, were used as primary antibody. After overnight incubation at room temperature, specimens were rinsed with PBS and incubated at room temperature for 1 h with secondary antibody conjugated to peroxidase (0.2 $\mu g\,ml^{-1}$). The specimens were then rinsed with PBS and colour developed in the presence diaminobenzidine (DAB) solution (DAKO). After washing, specimens were counterstained with Meyer's haematoxyline (Sigma). Immunostaining of all samples was performed at the same conditions of antibody reaction and DAB exposure.

Evaluation of immunohistochemistry. The intensity of immunoreactivity for MIA2 was classified with four grades: grade 0 was no immunoreactivity, grade 1 was weak, grade 2 was moderate, and grade 3 was strong immunoreactivity (Figure 1C–F). Cases with grade 2–3 immunoreactivity were judged as positive for MIA2 expression. Infiltration pattern of lymphocytes was classified in three patterns (Figure 3). Grade A is the scattered infiltration of lymphocytes at only the outside of tumour nests. Grade B is intermediate infiltration of lymphocytes at the outside and inside of tumour nests. Grade C is marked infiltration of lymphocytes at the outside and inside of tumour nests.

Cell lines and cell culture. HSC3 (drives from metastatic focus of human tongue SCC), HSC4 (derived from primary tumour of the same case of HSC3), and KON (derived from nodal metastatic focus of human oral floor cell lines) were purchase from Health Science Research Resources Bank (Osaka, Japan) were used. MOLT-3 T-lymphoblastic leukaemia cell line was purchased from Dainihon Pharmaceutical, Tokyo, Japan. Cells were maintained in Dulbecco's modified Eagle's medium (DMEM) (Wako Pure Chemical, Osaka, Japan) supplemented with 10% FBS (Sigma) in 5% CO_2 and 95% air at 37 °C. For MIA2 inhibition, antibody to MIA2 (Abcam, 1 $\mu g\,ml^{-1}$) was added to culture medium and cultured for 48 h. For the control, rabbit serum (DAKO, 1 $\mu g\,ml^{-1}$) was used. Extracellular signal-regulated kinase (ERK) inhibitor (Calbiochem-Novabiochem, Darmstadt, Germany), p38 mitogen-activated protein kinase (MAPK) inhibitor (SB239063, Sigma), and c-Jun N-terminal kinase (JNK) inhibitor (SP600125, Biomol, Hamburg, Germany) were treated for 24 h. Apoptosis were assessed by staining with Hoechst33258 fluorescent dye (Wako). Number of apoptotic cells was counted by observation of 500 cells.

Coculture of OSCC cell with T lymphocytes. HSC3 cells and (5×10^2) and MOLT-4 cells (5×10^2) were seeded and cultured for 24 h in 96-well culture dish. Cells fixed with 4% paraformaldehyde for 6 h at 4 °C were treated with peroxidase-conjugated anti-CD3 antibody (DAKO, 0.5 $\mu g\,ml^{-1}$) for 30 min at 37 °C. Cells were treated with tetramethylbenzidin (DAKO) after rinse with PBS for colour development. The reaction was stopped with 0.2 N H_2SO_4 and the colour concentration was measured at OD 450 nm. Anti-MIA2 antibody (Abcam) was used for antibody treatment with a concentration of 0.5 $\mu g\,ml^{-1}$.

Short interfering RNA. Stealth Select RNAi (short interfering RNA, siRNA) for *MIA*, *MIA2*, *ITGA4* and *ITGA5*, and negative siRNA (control siRNA) were purchased from Invitrogen (Carlsbad, CA, USA). Short interfering RNAs (20 nM) were transfected with Lipofectamine2000 (Invitrogen) according to the manufacture's recommendations. Effect of siRNA was confirmed by real-time RT–PCR.

Transwell infiltration assay of T lymphocytes. Our previous method was modified (Kuniyasu *et al*, 2004). HSC3 cells (1×10^4) were seeded on the bottom of the insert well coated with fibronectin (pore size 3 μm; diameter 5 mm, Becton-Dickinson, Bedford, MA, USA), which was set on the well and exchanged medium to DMEM with 2% bovine serum albumin (BSA; Sigma). MOLT-3 cells (5×10^3), which were surface-labelled with PKH26 chemifluorescent dye (Zynaxis, Malvern, PA, USA), were seeded on each insert using 2% BSA-DMEM. After 6-h incubation, infiltrating MOLT-3 cells were counted as fluorescence-positive cells in the lower chamber by an autocytometer (Sysmecs, Kobe, Japan).

Quantitative reverse transcription–PCR. The extraction of total RNA was carried out using RNeasy Mini Kit (Qiagen Genomics, Bothell, WA, USA), and total RNA (1 μg) was synthesised with the ReverTra Ace-α-RT Kit (Toyobo, Osaka, Japan). Quantitative reverse transcription–PCR (qRT–PCR) was performed by StepOne Real-Time PCR Systems (Applied Biosystems, Foster City, CA, USA) using Fast SYBR Green Master Mix (Applied Biosystems), and analysed by the relative standard curve quantification method (Livak and Schmittgen, 2001). PCR condition was set according to

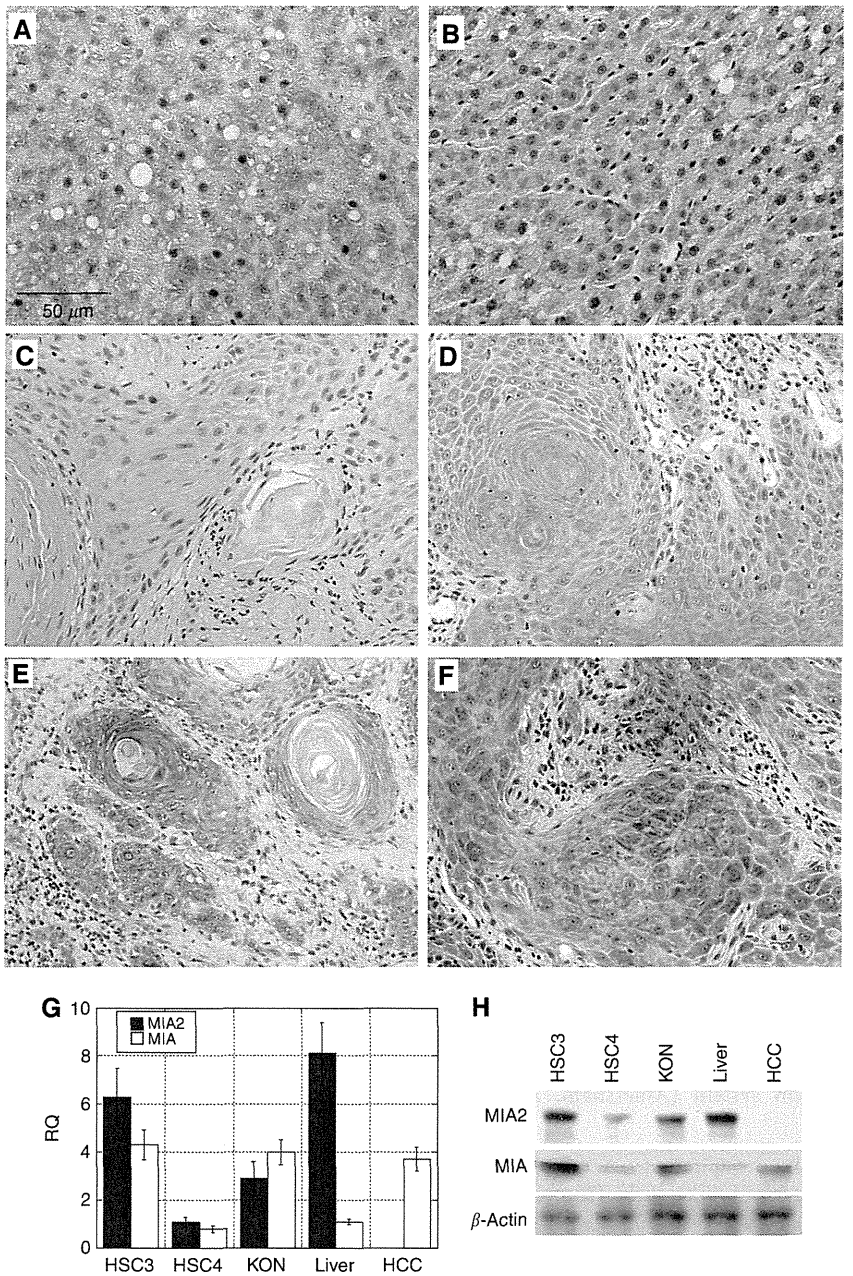

Figure 1. Expression of melanoma inhibitory activity 2 (MIA2) in oral squamous cell carcinoma (OSCC). (**A**) MIA2 immunoreactivity in a non-tumorous, non-hepatitis liver specimen that was used as a positive control. The cytoplasm of the hepatocytes in an acute hepatitis case showed high-grade MIA2 immunoreactivity. (**B**) A specimen of human hepatocellular carcinoma was examined as a negative control. It showed no MIA2 immunoreactivity. (**C–F**) Immunohistochemical analysis of MIA2 expression in OSCC cases. Positive immunoreactivity was seen in the cytoplasm of the cancer cells. (**C**) A well-differentiated stage I OSCC case (T1 N0 M0) showed no MIA2 immunoreactivity (grade 0). (**D**) A well-differentiated stage II OSCC case (T2 N0 M0) showed weak MIA2 immunoreactivity (grade 1). (**E**) A well-differentiated stage IV OSCC case (T4 N0 M0) showed moderate MIA2 immunoreactivity (grade 2). (**F**) A well-differentiated stage III OSCC case (T3 N1 M0) showed strong MIA2 immunoreactivity (grade 3). Bar, 50 μm. MIA2 and MIA mRNA expressions were examined using qRT–PCR (**G**) and immunoblotting (**H**) in the highly metastatic cell line HSC3, low metastatic cell line HSC4, and KON cell line derived from metastatic lymph nodes cells. The tissues of non-tumorous, non-hepatitis liver and hepatocellular carcinoma were examined as positive and negative control, respectively, for MIA2 expression. Melanoma inhibitory activity expression was also examined. β-Actin served as the loading control.

the provider's instructions. ACTB mRNA was amplified for internal control (GenBank accession No. NM 001101). Each amplification reaction was evaluated by a melting curve analysis. For visualising PCR products, agarose gel electrophoresis was performed with ethidium bromide staining.

Preparation of conditioned medium. HSC3 cells were cultured in 2% BSA-DMEM for 12 h by treatment with MIA2 siRNA or anti-MIA2 antibody (Abcam, 0.5 μg ml^{-1}). Then the conditioned medium was filtered with a 0.2-μm-filter (Becton-Dickinson Labware).

Immunoblotting. Cell lysate was extracted as previously described (Kuniyasu *et al*, 2002). Cell lysate (50 μg) was separated by 12.5% SDS–PAGE. Proteins were blotted onto nitrocellulose membrane electronically. The membrane was treated with primary

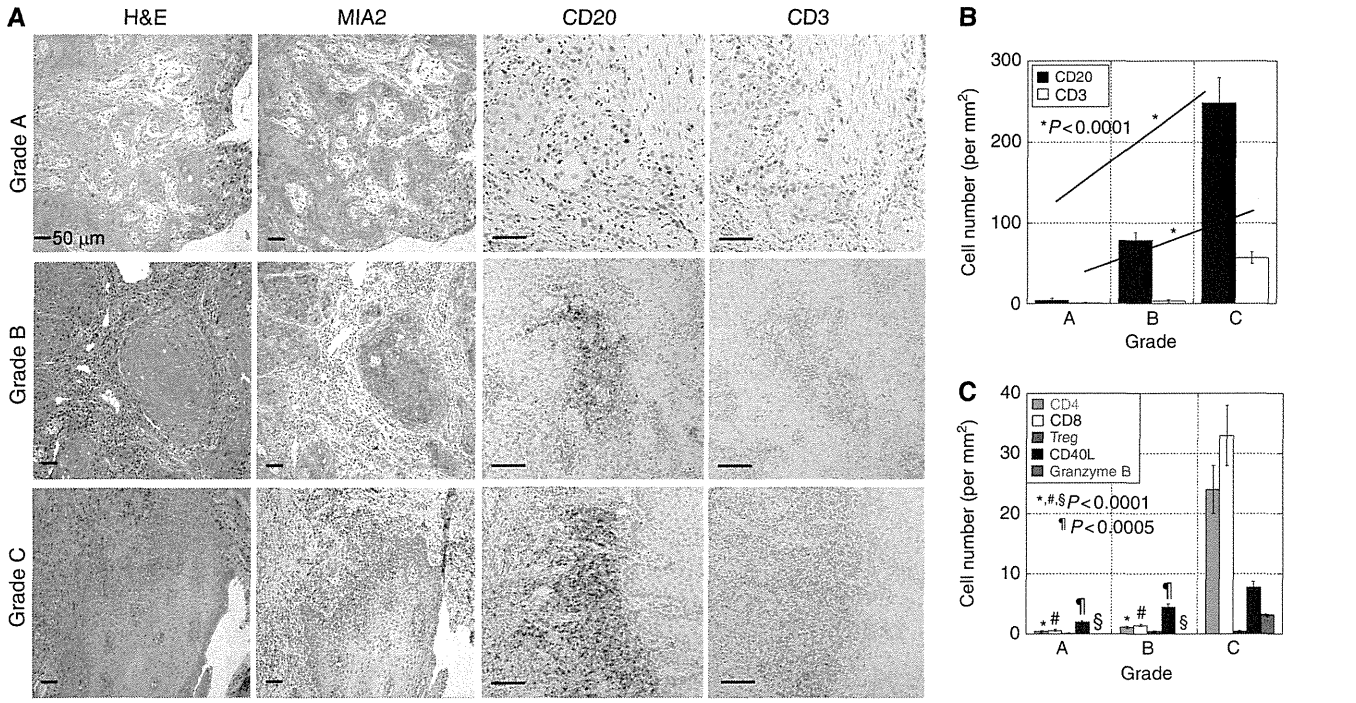

Figure 2. Infiltration pattern of lymphocytes in oral squamous cell carcinoma (OSCC). (**A**) The infiltration pattern of lymphocytes in OSCC was classified into three patterns: grade A, scattered infiltration of lymphocytes at only the outside of the tumour nests; grade B, intermediate infiltration of lymphocytes at the outside and inside of tumour nests; and grade C, marked infiltration of lymphocytes at the outside and inside of the tumour nests. Bar, 50 μm. Melanoma inhibitory activity 2 expression and CD20(+) and CD3(+) lymphocytes were examined by immunohistochemistry in each case. (**B**) Number of infiltrating CD3(+) and CD20(+) cells in tumours of 93 OSCC cases. (**C**) Number of infiltrating CD4(+), CD8(+), FOXP3(+) regulatory T cell (Treg), and CD40L(+)-activated CD4 cells in tumours of 93 OSCC cases. Error bar, s.d.

antibodies to MIA and MIA2 (Abcam), integrin α4, integrin α5, phosphorylated ERK1/2, phosphorylated JNK, phosphorylated p38, VEGF, VEGF-C, and VEGF-D (Santa-Cruz Biotechnology, Santa-Cruz, CA, USA). An α-tubulin antibody was used to assess the levels of protein loaded per lane (Oncogene Research Products, Cambridge, MA, USA). The immune complex was visualised with an ECL western-blot detection system (Amersham, Aylesbury, UK).

Immunoprecipitation. Immunoprecipitation was performed according to the method described previously (Kuniyasu *et al*, 2001). The lysates were pre-cleaned in lysis buffer with protein A/G agarose (Santa-Cruz) for 1 h at 4 °C and subsequently centrifuged. The supernatants were incubated with precipitation antibody and protein A/G agarose for 3 h at 4 °C. Precipitates were collected by centrifugation and washed five times with lysis buffer. Precipitates solubilised with sample buffer (Sigma, 40 μg) were subjected to immunoblot analysis. For precipitation, antibodies to integrin α4 and integrin α5 (Santa-Cruz) were used. For detection, antibodies to MIA and MIA2 (Abcam) were used.

Statistical analysis. Statistical analysis of experimental data was done by Mann–Whitney *U*-test and χ^2 test. The statistical significance was defined as a two-sided *P*-value of <0.05.

RESULTS

MIA2 expression in OSCC. MIA2 expression was examined by immunohistochemistry in 93 cases of OSCC (Table 1). Melanoma inhibitory activity 2 immunoreactivity was detected in the cytoplasm of hepatocytes and cancer cells of OSCC (Figure 1A and C–F). In contrast, HCC cells did not show MIA2 immunoreactivity (Figure 1B). Cases with grade 2 or 3 immunoreactivity were judged as positive for MIA2 expression.

We next compared the MIA2 expression in HSC3 (high metastatic cell line), HSC4 (low metastatic cell line), and KON (metastatic lymph nodes cell line) using qRT–PCR and immunobloting (Figure 1G and H). The MIA2 expression level was higher in HSC3 than in HSC4 and KON. The MIA2 expression in OSCC cells was compared with the MIA expression. The MIA2 and MIA were expressed in all OSCC cell lines at various levels.

Relation of MIA2 expression with clinicopathological parameters. MIA2 expression was observed in 62 (66.7%) of the 93 cases and was associated with T classification (tumour expansion) and nodal metastasis (Table 1). Of the 22 cases of local invasion (T3 or T4), 14 (63.6%) expressed MIA2, whereas only 18 (25.3%) of the 71 cases of early cancer (T1 or T2) expressed MIA2 ($P=0.0017$). Of the 30 cases with nodal metastasis (n+), 17 (56.7%) showed MIA2 expression, whereas only 15 (23.8%) of the 63 cases without nodal metastasis (n−) expressed MIA2 ($P=0.0025$). However, no significant relationship was found between MIA2 grading and the other parameters including age, sex, primary site, clinical stage, histological differentiation, and tumour recurrence.

MIA2 expression and lymphocyte infiltration. The infiltration pattern of the lymphocytes was classified into three patterns (Figure 2A). Grade C showed the most pronounced lymphocyte infiltration among the three patterns, whereas grade A showed mild and remote lymphocytes infiltration. As shown in Table 2, MIA2 expression was inversely associated with lymphocyte infiltration. Of the 31 grade A cases, 17 (54.8%) showed MIA2 expression, whereas only 4 (12.9%) of the 31 grade C cases expressed MIA2. This result suggests that MIA2 might inhibit intratumoral lymphocyte infiltration.

To examine the detail of MIA2 effect on lymphocytes, subpopulation of them was examined (Figure 2A–C). CD3+ or CD20+ lymphocytes were markedly decreased in grade A case

Table 1. Correlation between MIA2 expression and clinicopathological characteristics of human oral squamous cell carcinoma

	MIA2 expression grade		
Parameters	**0–1**	**2–3**	***P*-value[a]**
Age (years)			
<60	17	9	
>60	44	23	NS
Sex			
Male	27	16	
Female	34	16	NS
Site			
Tongue	35	17	
Gingiva	16	11	
Buccal mucosa	6	3	
Other	4	1	NS
Differentiation[b]			
Well	37	25	
Mod	22	7	
Poor	2	0	NS
T factor[c]			
T1, T2	53	18	
T3, T4	8	14	0.0017
Nodal metastasis			
(−)	48	15	
(+)	13	17	0.0019
Pathologic stage[c]			
I, II	41	17	
III, IV	20	15	NS
Recurrence			
(−)	32	16	
(+)	20	12	NS

Abbreviations: MIA2 = melanoma inhibitory activity 2; NS = nonsignificant.
[a]Fisher exact *t*-test.
[b]Histological differentiation: well, well-differentiated; mod, moderately differentiated; poor, poorly differentiated.
[c]According to the tumour, node, metastasis classification.

Table 2. Relationship between MIA2 expression and infiltration pattern of lymphocytes in oral squamous cell carcinoma

	MIA2 expression	
Lymphocyte infiltration pattern	**Grade 0–1**	**Grade 2–3**
Grade A	14 (23%)	17 (53%)
Grade B	20 (33%)	11 (34%)
Grade C	27 (44%)	4 (13%)

Abbreviation: MIA2 = melanoma inhibitory activity 2. $P = 0.00248$ (χ^2 test).

(Figure 2A). As shown in Figure 2B, both CD3+ and CD20+ lymphocytes were decreased as the grade; however, decrease of CD3+ lymphocytes was more pronounced than that of CD20 lymphocytes. Next the sub-population of T lymphocytes was examined (Figure 2C). In grade A and B, CD4+, CD8+, and granzyme B+ T lymphocytes were markedly decreased than that in grade C; however, CD40L+ lymphocytes showed more modest association with the grade. The number of regulatory T lymphocytes was not associated with the grade.

Effect of MIA2 knockdown in the OSCC cell lines. We next performed MIA2 knockdown by siRNA treatment to examine the roles of MIA2 on cell growth, invasion, and apoptosis in HSC3 cells (Figure 3). Melanoma inhibitory activity 2 siRNA treatment decreased the levels of mRNA and protein in HSC3 cells (Figure 3A). Compared with the control siRNA treatment, cell invasion and anti-apoptotic survival were reduced by MIA2 siRNA treatment ($P = 0.0417$ and $P = 0.018$, respectively). Cell growth with MIA2 siRNA treatment was not significantly different from that before the treatment.

Effect of MIA2 depletion on lymphocytes infiltration. HSC3 cells and MOLT-3 lymphocytes were cocultured to confirm the lymphocyte inhibitory effect of MIA2 (Figure 4A). The number of MOLT-3 cells was not affected by the coculturing. Next, we conducted a trans-cell layer assay using an insert chamber (Figure 4C–D). The MIA2 protein levels in the cultured medium of HSC3 cell were examined (Figure 4B). Melanoma inhibitory activity 2 knockdown and absorption by anti-MIA2 antibody depleted MIA2 protein in the medium. The number of MOLT-3 lymphocytes that passed through the HSC3 cell layer at the bottom of the insert was then counted. The infiltrating cell number was increased by MIA2 depletion by MIA2 knockdown and the antibody treatment.

Effect of MIA2 knockdown on the VEGF, VEGF-C, and VEGF-D expressions in the HSC3 OSCC cells. MIA is a known angiogenic and lymphangiogenic factor inducing VEGF and VEGF-D (Sasahira *et al*, 2008, 2010). As such, we examined the effect of MIA2 knockdown on the levels of mRNA and protein of VEGF, VEGF-C, and VEGF-D and compared it with the effect of MIA knockdown in HSC3 cells. Treatment with specific siRNAs to MIA2 or MIA decreased the levels of mRNA and protein in the HSC3 cells (Figure 5A and B). The HSC3 cells after MIA2 knockdown showed modestly inhibited VEGF and VEGF-C expressions compared with those after MIA knockdown (Figure 5C and D). In contrast, the HSC3 cells after MIA2 knockdown showed VEGF-D downregulation similar to that in cells after MIA knockdown (Figure 5E). It is interesting that the double knockdown of MIA2 and MIA showed less of an inhibitory effect on VEGF and VEGF-C downregulation, whereas it showed a greater inhibitory effect on VEGF-D downregulation (Figure 5C–E). Finally, the HSC3 cells after MIA or MIA2 knockdown were treated with ERK1/2 and p38 inhibitors (Figure 5F). In both MIA and MIA2 knockdown, VEGF-C expression was decreased by p38 inhibition, whereas VEGF-D was decreased by ERK1/2 inhibition.

Comparison of the role of integrins in MIA2 function. MIA is a known interacting partner of integrins α4 and α5 (Bauer *et al*, 2006). As such, we examined the physical association between MIA2 and the integrins (Figure 6A). The HSC3 lysates showed co-precipitation between MIA2 and integrin α4 or α5 as with MIA. Melanoma inhibitory activity 2 showed higher affinity with integrin α4 than that with integrin α5, unlike MIA in the HSC3 cells. Knockdown of the expression of integrins α4 (*ITGA4*) and α5 (*ITGA5*) was confirmed in the HSC3 cells (Figure 1B). Using the knockdown system, the phosphorylation status of the MAPK family was examined (Figure 6C–E). In the MIA-knockdown HSC3 cells, which expressed *MIA2*, *ITGA4* knockdown decreased p38 phosphorylation. In contrast, *ITGA5* knockdown decreased the phosphorylation of p38 and JNK. In MIA2-knockdown HSC3 cells

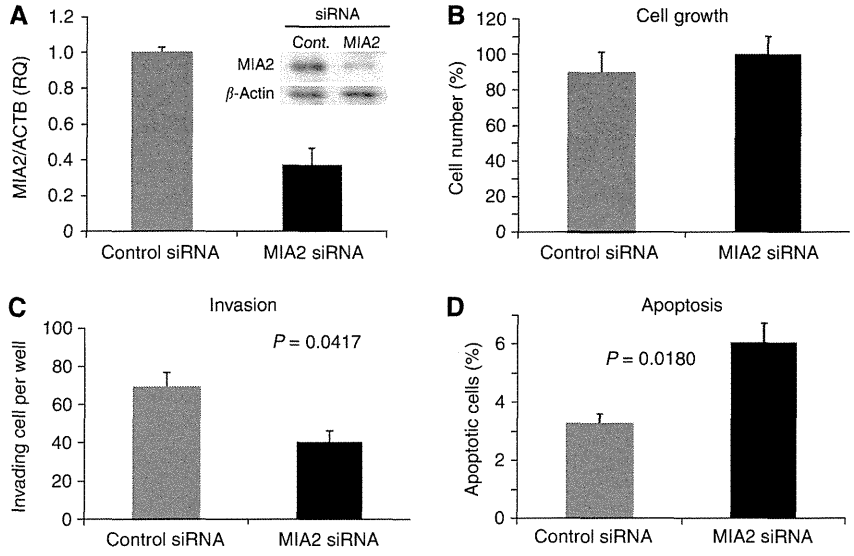

Figure 3. Effect of knockdown of melanoma inhibitory activity 2 (MIA2) in oral squamous cell carcinoma (OSCC) cell lines. (**A**) The effect of MIA2 siRNA treatment on MIA2 mRNA expression in HSC3 cells. Melanoma inhibitory activity 2 protein levels were also shown in the inset. The effects of MIA2 knockdown on cell growth (**B**), invasion (**C**), and apoptosis (**D**) in the HSC3 cells. Error bar, s.d.

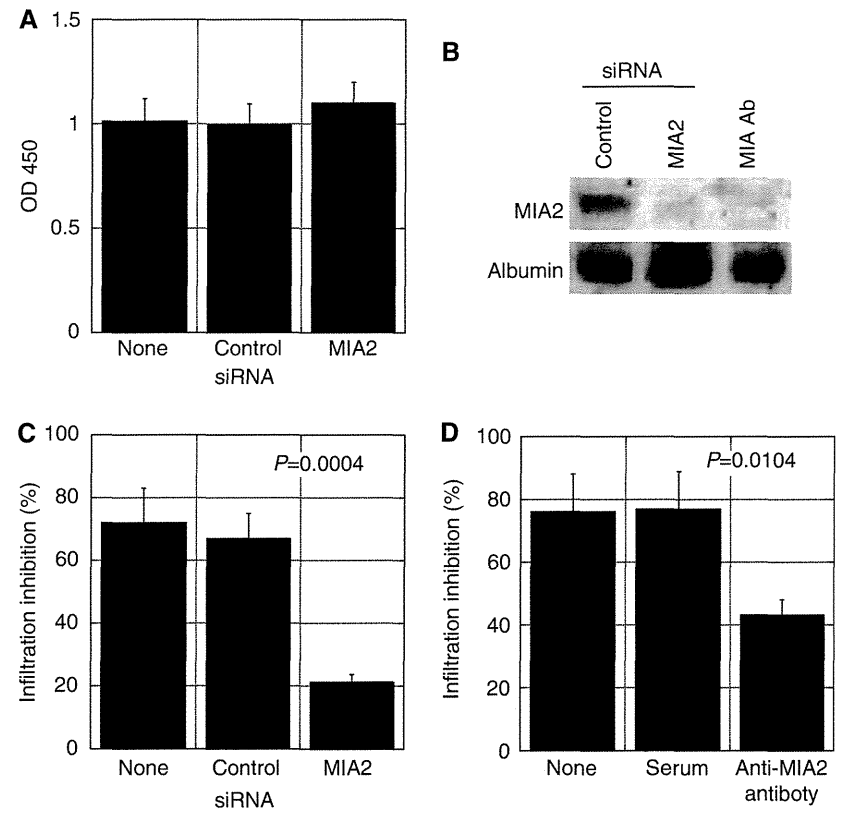

Figure 4. Transwell infiltration of MOLT-3 lymphocytes through an HSC3 cell layer. (**A**) The HSC3 and MOLT-3 cells were cocultured with melanoma inhibitory activity 2 (MIA2) siRNA or control siRNA. (**C**, **D**) Inhibition of transwell infiltration of MOLT-3 cells. The number of MOLT-3 cells infiltrating through the HSC3 cell layer at the bottom of the insert was compared with that using the insert without cell layer. (**C**) The cells were exposed to MIA2 siRNA or control siRNA. (**B**) The cells were treated with control serum or anti-MIA2 antibody. Error bar, s.d.

expressing *MIA*, knockdown of *ITGA4* and *ITGA5* decreased the phosphorylation of p38 and JNK.

Finally, we examined the effect of *ITGA4* or *ITGA5* knockdown and MAPK inhibitors on apoptosis in MIA-knockdown HSC3 cells (Figure 6F and G). *ITGA4* knockdown increased apoptosis, whereas *ITGA5* knockdown decreased apoptosis. The inhibition of JNK decreased apoptosis, whereas inhibition of p38 increased apoptosis. These findings suggest that JNK activation by MIA2 through integrin α5 might induce apoptosis. In contrast, p38 activation through integrin α4 and α5 might suppress apoptosis.

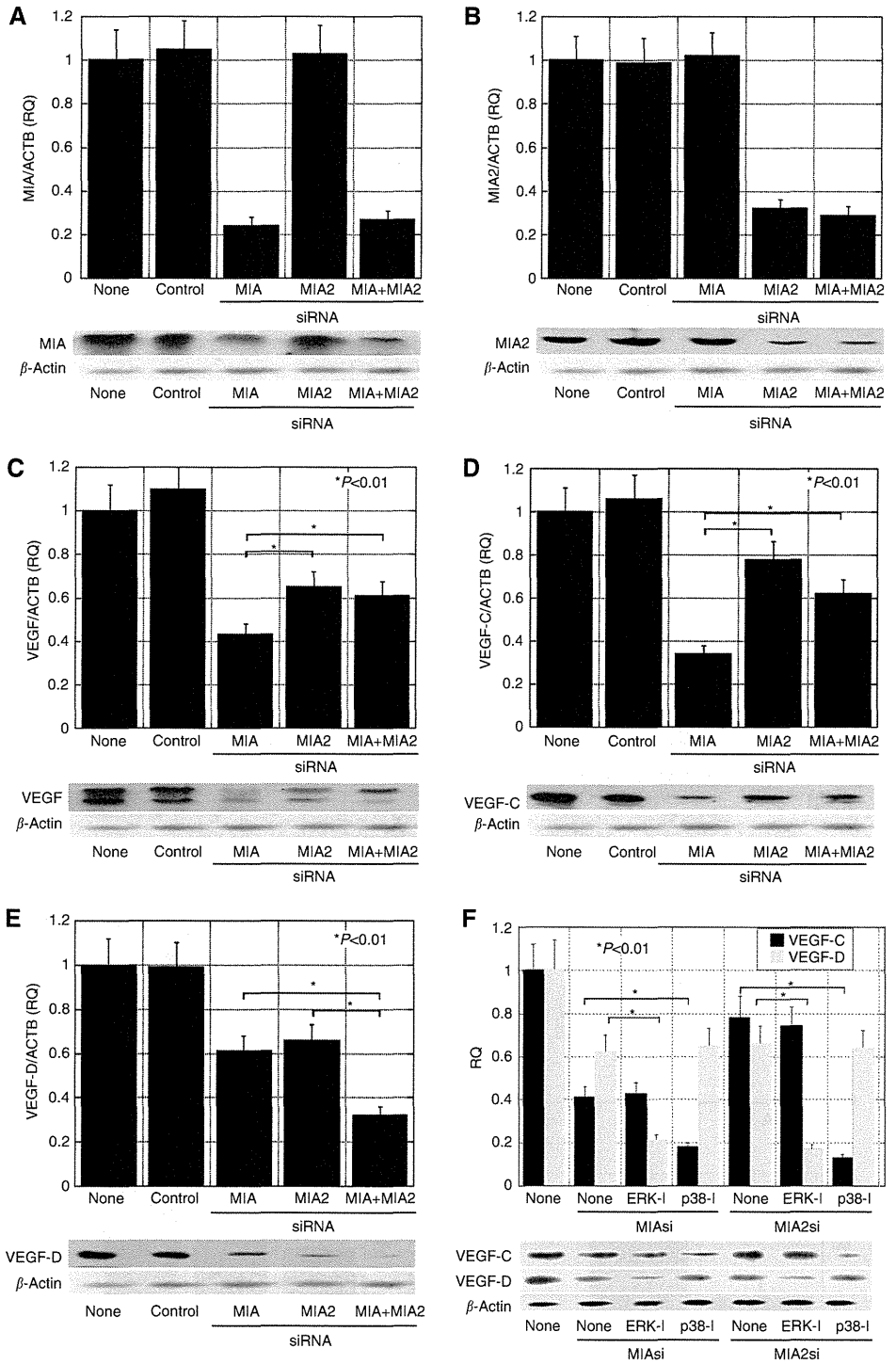

Figure 5. Effect of knockdown of melanoma inhibitory activity 2 (MIA2) and/or MIA on vascular endothelial growth factor (VEGF), VEGF-C, and VEGF-D expressions in the HSC3 cells. Effect of knockdown of MIA and/or MIA2 on the expression of MIA (**A**) and MIA2 (**B**) was confirmed using qRT–PCR and immunoblotting. The expressions of VEGF (**C**), VEGF-C (**D**), and VEGF-D (**E**) were examined by qRT–PCR and immunoblotting in HSC3 cells with knockdown of MIA, MIA2, or MIA + MIA2. (**F**) Expression of VEGF-C and -D was examined using qRT–PCR and immunoblotting in MIA- or MIA2-knockdown HSC3 cells treated with inhibitors of ERK1/2 (ERK-I) or p38 (p38-I). Error bar, s.d.

DISCUSSION

MIA2 is isolated as a second member of the MIA homologous gene family. Melanoma inhibitory activity is a protumoral factor in the progression and metastasis of malignant melanoma and OSCC. In contrast, MIA2 is downregulated in HCC, which suggests that MIA2 has a putative tumour-suppressive function. It is interesting that our data on OSCC suggest that MIA2 might act as a protumoral factor similar to MIA.

In clinical study, MIA2 expression was associated with tumour expansion, nodal metastasis, less lymphocyte infiltration, and advanced-stage OSCC. Highly metastatic OSCC cell lines expressed MIA2 at higher levels than a low metastatic cell line. Melanoma inhibitory activity 2 knockdown was associated with inhibition of cell invasion, anti-apoptotic survival, and VEGF, VEGF-C, and

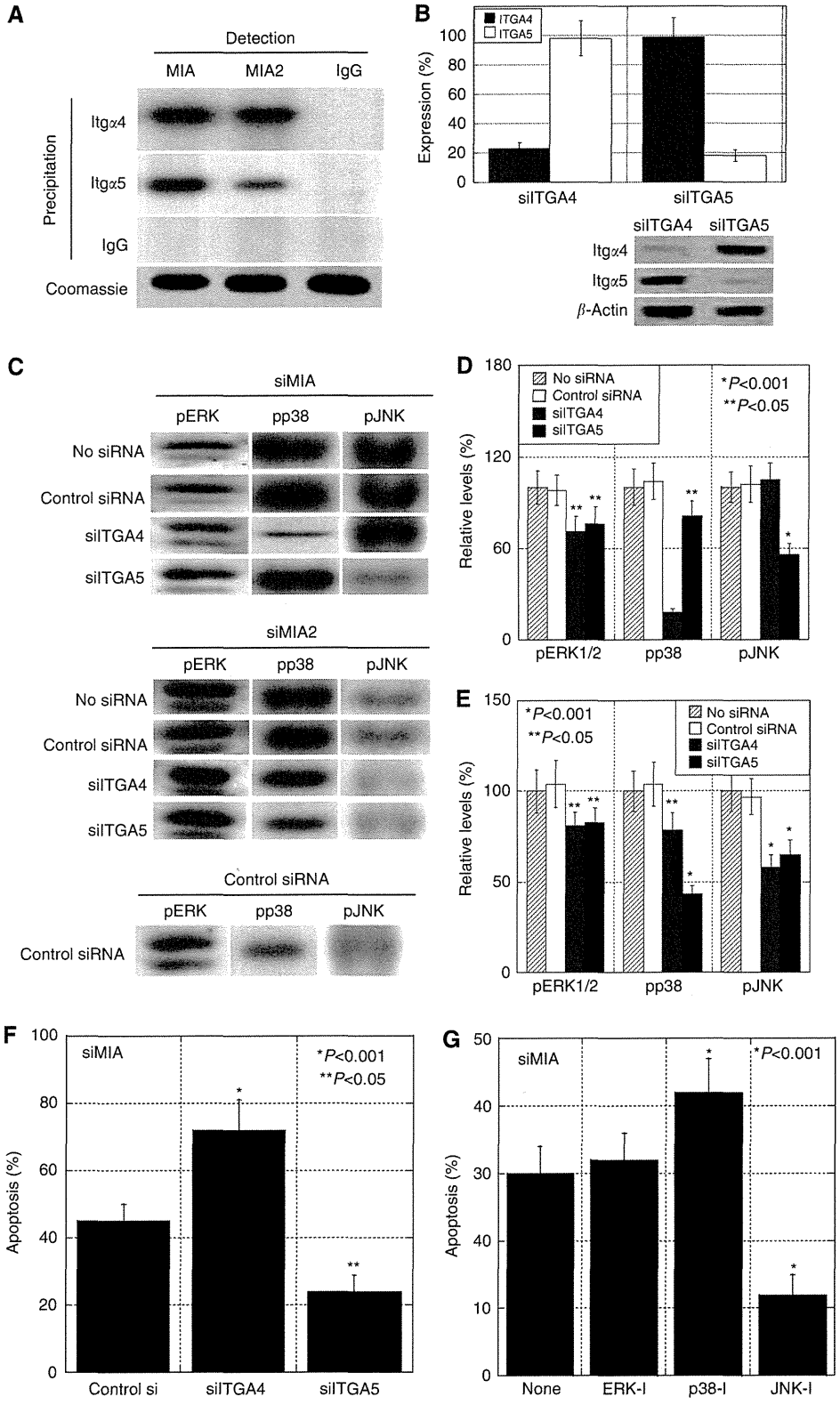

Figure 6. Roles of integrin and mitogen-activated protein kinase (MAPK) in melanoma inhibitory activity 2 (MIA2) function. Immunoprecipitation of the HSC3 cell lysate precipitated with antibodies to integrin α4 (Itgα4) or integrin α5 (Itgα5), detected with antibodies to MIA or MIA2. Precipitation and detection by IgG was done for negative control. Coomassie blue staining of slot blot samples served as a control for protein content. (**B**) Knockdown of integrin α4 (*ITGA4*) or integrin α5 (*ITGA5*) was examined using qRT–PCR and immunoblotting. (**C**) Phosphorylation levels of MAPK families were examined by immunoblotting in HSC3 cells with concurrent knockdown of MIA or MIA2 and *ITGA4* or *ITGA5*. (**D**, **E**) Phosphorylation levels of the MAPK families were semiquantified with standardisation to those in HSC3 cells untreated with siRNA. (**F**, **G**) Effect of knockdown of *ITGA4* or *ITGA5*, p38 inhibitor (p38-I), or JNK (JNK-I) on trichostatin A-induced apoptosis. The percentage of apoptotic cells to 500 counted cells was calculated. Error bar, s.d.

VEGF-D expressions. These results suggest that MIA2 increases invasion, survival and angiogenesis, and inhibits host anticancer immunity.

MIA2 shares protein homology, including *src* homology domain-3, with MIA (Bosserhoff *et al*, 2004). The immunoprecipitation assay in the present study showed that MIA2 and MIA are bound to integrins α4 and α5; however, MIA2 showed higher affinity to integrin α4 than to integrin α5. Melanoma inhibitory activity activated p38 and JNK through integrins α4 and α5, whereas MIA2 activated p38 through integrin α4 and α5, and activated JNK through integrin α5. Moreover, the MIA2-integrin α5-JNK signal increased apoptosis, whereas the MIA2-integrin α4-p38 signal decreased apoptosis.

MIA2 had a pro-angiogenic role by increasing VEGF family expression. The increment was modest compared with that by MIA; however, MIA2 showed a less pronounced increase in VEGD and VEGF-C than that by MIA. In contrast, VEGF-D upregulation by MIA2 was at the same level to that by MIA. The VEGF-C upregulation signal by MIA2 was carried through p38, which is also associated with MIA-induced VEGF family upregulation (Sasahira *et al*, 2008, 2010). In contrast, the VEGF-D upregulation signal by MIA2 was carried through ERK1/2 as found in that by MIA (Sasahira *et al*, 2008). Coexpressed MIA and MIA2 was found in most OSCC cell lines and human OSCC tumours, and expression of the VEGF family might be affected by MIA and MIA2 by a synergic (as show in VEGF-D) or nonsynergic (as shown in VEGF and VEGF-C) manner.

MIA2 expression was inversely associated with lymphocyte infiltration into the tumours. Melanoma inhibitory activity binds to integrin α4, which is expressed in the host immune cells and suppresses lymphokine-activated killer cell cytotoxicity (Jachimczak *et al*, 2005). Our data showed that MIA2 also bound to integrin α4, which might inhibit lymphocyte infiltration into the tumour. The coculture of HSC3 cells and MOLT-3 lymphocytes did not induce cell death in MOLT-3 cells, an observation suggesting that MIA2 possesses no cytotoxic effect on lymphocytes. As MIA binds to fibronectin to induce tumour cell detachment from the extracellular matrix (Bosserhoff *et al*, 2003b), MIA2 might also bind to fibronectin. Fibronectin induces chemotaxis of T lymphocytes in combination with stromal cell-derived factor 1α (Savino *et al*, 2002). The masking of fibronectin by MIA or MIA2 might inhibit chemotaxis of the T lymphocytes.

Among lymphocyte sub-population, decrease of CD4+, CD8+, and granzyme B+ lymphocytes was most significantly associated with the grade, and subsequently with MIA2 expression, which suggest that MIA2 might inhibit cytotoxic T lymphocytes mainly. No alteration in the number of regulatory T lymphocytes might enhance their immune-suppressive effect through decrease of other types of T lymphocytes. Importantly, CD20+ B lymphocytes also showed a decrease in association with grade or MIA2 expression. The decrease in association of CD40L+ T lymphocytes, which are associated with humoral immune activity, might decrease the association of B lymphocytes (Lederman *et al*, 1996).

MIA is regulated by HMGB1 via a highly conserved region promoter element in the 5′-flanking region of the *MIA* gene (Poser *et al*, 2003). We reported previously that HMGB1 affected MIA expression in OSCC cells (Sasahira *et al*, 2008). Comparison of MIA and MIA2 protein levels showed no association between them. Therefore, MIA2 might not be regulated by HMGB1. In the liver, MIA2 expression is transcriptionally regulated by HNF-1 (Bosserhoff *et al*, 2003a, 2004; Hellerbrand *et al*, 2008). Hepatocyte nuclear factor-1A expression is reported in human OSCC (O'Donnell *et al*, 2005), suggesting that it induces MIA2 expression in OSCC. Prostaglandin E2 (PGE2) activates T-cell factor (same as HNF)-dependent transcription (Shao *et al*, 2005). Prostaglandin E2 is highly involved in tumour growth in the head and neck cancers (Abrahao *et al*, 2010). Therefore, MIA2 might be a common tumour-associated factor in OSCC.

Melanoma inhibitory activity 2 is expressed at high levels and acts as an antitumor factor in the liver (Bosserhoff *et al*, 2004; Hellerbrand *et al*, 2005, 2008). Melanoma inhibitory activity 2 expression is repressed in hepatitis, cirrhosis, and hepatoma, which is associated with cell proliferation (Hellerbrand *et al*, 2008; Xu *et al*, 2011). In contrast, MIA2 acts as a protumoral factor in OSCC. Melanoma inhibitory activity 2 affinity to the MIA receptors, integrins α4 and α5, suggests that MIA2 might act as a competitive inhibitor of MIA. Otherwise, HCC cells express integrin α4 at a markedly lower level than integrin α5 (Fu *et al*, 2010). These features in the liver suggest that MIA2 might act as a pro-apoptotic factor through integrin α5. Moreover, OSCC concurrently expressed MIA2 with MIA at high frequency (87%, data not shown). The overlapping of signals from MIA2 and MIA through integrin α4 and α5 might result a protumoral role in OSCC. Melanoma inhibitory activity is expressed in the liver at low levels (Su *et al*, 2002). A lack of synergism between MIA and MIA2 also might emphasise a pro-apoptotic role in the liver.

These data suggest that MIA2 might act as a protumoral factor that was influenced by concurrent expression of MIA, receptor integrin expression patterns, and activation pattern of MAPK family in OSCC. The frequent expression in OSCC suggests that MIA2 is a relevant target for cancer treatment.

ACKNOWLEDGEMENTS

This work was supported in part by Grant-in-Aid for Scientific Research from Japan Society for the Promotion of Science, Japan, and Grant-in-Aid for Scientific Research from Ministry of Health, Labour and Welfare, Japan.

CONFLICT OF INTEREST

The authors declare no conflict of interest.

REFERENCES

Abrahao AC, Castilho RM, Squarize CH, Molinolo AA, dos Santos-Pinto Jr D, Gutkind JS (2010) A role for COX2-derived PGE2 and PGE2-receptor subtypes in head and neck squamous carcinoma cell proliferation. *Oral Oncol* **46**(12): 880–887.

Adams RH, Alitalo K (2007) Molecular regulation of angiogenesis and lymphangiogenesis. *Nat Rev Mol Cell Biol* **8**(6): 464–478.

Avraamides CJ, Garmy-Susini B, Varner JA (2008) Integrins in angiogenesis and lymphangiogenesis. *Nat Rev Cancer* **8**(8): 604–617.

Bauer R, Humphries M, Fassler R, Winklmeier A, Craig SE, Bosserhoff AK (2006) Regulation of integrin activity by MIA. *J Biol Chem* **281**(17): 11669–11677.

Beck Jr L, D'Amore PA (1997) Vascular development: cellular and molecular regulation. *FASEB J* **11**(5): 365–373.

Bosserhoff AK, Buettner R (2002) Expression, function and clinical relevance of MIA (melanoma inhibitory activity). *Histol Histopathol* **17**(1): 289–300.

Bosserhoff AK, Moser M, Buettner R (2004) Characterization and expression pattern of the novel MIA homolog TANGO. *Gene Expr Patterns* **4**(4): 473–479.

Bosserhoff AK, Moser M, Scholmerich J, Buettner R, Hellerbrand C (2003a) Specific expression and regulation of the new melanoma inhibitory activity-related gene MIA2 in hepatocytes. *J Biol Chem* **278**(17): 15225–15231.

Bosserhoff AK, Stoll R, Sleeman JP, Bataille F, Buettner R, Holak TA (2003b) Active detachment involves inhibition of cell-matrix contacts of malignant melanoma cells by secretion of melanoma inhibitory activity. *Lab Invest* **83**(11): 1583–1594.

Ferlay J, Shin HR, Bray F, Forman D, Mathers C, Parkin DM (2010) Estimates of worldwide burden of cancer in 2008: GLOBOCAN 2008. *Int J Cancer* **127**(12): 2893–2917.

Fu BH, Wu ZZ, Qin J (2010) Effects of integrins on laminin chemotaxis by hepatocellular carcinoma cells. *Mol Biol Rep* **37**(3): 1665–1670.

Hellerbrand C, Amann T, Schlegel J, Wild P, Bataille F, Spruss T, Hartmann A, Bosserhoff AK (2008) The novel gene MIA2 acts as a tumour suppressor in hepatocellular carcinoma. *Gut* **57**(2): 243–251.

Hellerbrand C, Bataille F, Schlegel J, Hartmann A, Muhlbauer M, Scholmerich J, Buttner R, Hofstadter F, Bosserhoff AK (2005) *In situ* expression patterns of melanoma inhibitory activity 2 in healthy and diseased livers. *Liver Int* **25**(2): 357–366.

Jachimczak P, Apfel R, Bosserhoff AK, Fabel K, Hau P, Tschertner I, Wise P, Schlingensiepen KH, Schuler-Thurner B, Bogdahn U (2005) Inhibition of immunosuppressive effects of melanoma-inhibiting activity (MIA) by antisense techniques. *Int J Cancer* **113**(1): 88–92.

Kademani D, Bell RB, Bagheri S, Holmgren E, Dierks E, Potter B, Homer L (2005) Prognostic factors in intraoral squamous cell carcinoma: the influence of histologic grade. *J Oral Maxillofac Surg* **63**(11): 1599–1605.

Kreppel M, Eich HT, Kubler A, Zoller JE, Scheer M (2010) Prognostic value of the sixth edition of the UICC's TNM classification and stage grouping for oral cancer. *J Surg Oncol* **102**(5): 443–449.

Kuniyasu H, Oue N, Wakikawa A, Shigeishi H, Matsutani N, Kuraoka K, Ito R, Yokozaki H, Yasui W (2002) Expression of receptors for advanced glycation end-products (RAGE) is closely associated with the invasive and metastatic activity of gastric cancer. *J Pathol* **196**(2): 163–170.

Kuniyasu H, Sasaki T, Sasahira T, Ohmori H, Takahashi T (2004) Depletion of tumor-infiltrating macrophages is associated with amphoterin expression in colon cancer. *Pathobiology* **71**(3): 129–136.

Kuniyasu H, Yasui W, Pettaway CA, Yano S, Oue N, Tahara E, Fidler IJ (2001) Interferon-alpha prevents selection of doxorubicin-resistant undifferentiated-androgen-insensitive metastatic human prostate cancer cells. *Prostate* **49**(1): 19–29.

Lederman S, Cleary AM, Yellin MJ, Frank DM, Karpusas M, Thomas DW, Chess L (1996) The central role of the CD40-ligand and CD40 pathway in T-lymphocyte-mediated differentiation of B lymphocytes. *Curr Opin Hematol* **3**(1): 77–86.

Livak KJ, Schmittgen TD (2001) Analysis of relative gene expression data using real-time quantitative PCR and the 2(− Delta Delta C(T)) Method. *Methods* **25**(4): 402–408.

Lopez-Graniel CM, Tamez de Leon D, Meneses-Garcia A, Gomez-Ruiz C, Frias-Mendivil M, Granados-Garcia M, Barrera-Franco JL (2001) Tumor angiogenesis as a prognostic factor in oral cavity carcinomas. *J Exp Clin Cancer Res* **20**(4): 463–468.

Matsuda T, Marugame T, Kamo K, Katanoda K, Ajiki W, Sobue T (2012) Cancer incidence and incidence rates in Japan in 2006: based on data from 15 population-based cancer registries in the monitoring of cancer incidence in Japan (MCIJ) project. *Jpn J Clin Oncol* **42**(2): 139–147.

Miyahara M, Tanuma J, Sugihara K, Semba I (2007) Tumor lymphangiogenesis correlates with lymph node metastasis and clinicopathologic parameters in oral squamous cell carcinoma. *Cancer* **110**(6): 1287–1294.

Nagler RM (2002) Molecular aspects of oral cancer. *Anticancer Res* **22**(5): 2977–2980.

O'Donnell RK, Kupferman M, Wei SJ, Singhal S (2005) Squamous cell carcinoma of the oral cavity with lymph node metastasis: NCBI Gene Expression Omnibus.

Poser I, Golob M, Buettner R, Bosserhoff AK (2003) Upregulation of HMG1 leads to melanoma inhibitory activity expression in malignant melanoma cells and contributes to their malignancy phenotype. *Mol Cell Biol* **23**(8): 2991–2998.

Sasahira T, Kirita T, Kurihara M, Yamamoto K, Bhawal UK, Bosserhoff AK, Kuniyasu H (2010) MIA-dependent angiogenesis and lymphangiogenesis are closely associated with progression, nodal metastasis and poor prognosis in tongue squamous cell carcinoma. *Eur J Cancer* **46**(12): 2285–2294.

Sasahira T, Kirita T, Oue N, Bhawal UK, Yamamoto K, Fujii K, Ohmori H, Luo Y, Yasui W, Bosserhoff AK, Kuniyasu H (2008) High mobility group box-1-inducible melanoma inhibitory activity is associated with nodal metastasis and lymphangiogenesis in oral squamous cell carcinoma. *Cancer Sci* **99**(9): 1806–1812.

Savino W, Mendes-da-Cruz DA, Silva JS, Dardenne M, Cotta-de-Almeida V (2002) Intrathymic T-cell migration: a combinatorial interplay of extracellular matrix and chemokines? *Trends Immunol* **23**(6): 305–313.

Shang ZJ, Li JR, Li ZB (2002) Circulating levels of vascular endothelial growth factor in patients with oral squamous cell carcinoma. *Int J Oral Maxillofac Surg* **31**(5): 495–498.

Shao J, Jung C, Liu C, Sheng H (2005) Prostaglandin E2 Stimulates the beta-catenin/T cell factor-dependent transcription in colon cancer. *J Biol Chem* **280**(28): 26565–26572.

Shintani S, Li C, Ishikawa T, Mihara M, Nakashiro K, Hamakawa H (2004) Expression of vascular endothelial growth factor A, B, C, and D in oral squamous cell carcinoma. *Oral Oncol* **40**(1): 13–20.

Su AI, Cooke MP, Ching KA, Hakak Y (2002) Large-scale analysis of the human transcriptome (HG-U95A): NCBI Gene Expression Omnibus.

Tsurusaki T, Kanda S, Sakai H, Kanetake H, Saito Y, Alitalo K, Koji T (1999) Vascular endothelial growth factor-C expression in human prostatic carcinoma and its relationship to lymph node metastasis. *Br J Cancer* **80**(1–2): 309–313.

Xu Y, Yang Y, Cai Y, Liu F, Liu Y, Zhu Y, Wu J (2011) The X protein of hepatitis B virus activates hepatoma cell proliferation through repressing melanoma inhibitory activity 2 gene. *Biochem Biophys Res Commun* **416**(3–4): 379–384.

Yonemura Y, Endo Y, Fujita H, Fushida S, Ninomiya I, Bandou E, Taniguchi K, Miwa K, Ohoyama S, Sugiyama K, Sasaki T (1999) Role of vascular endothelial growth factor C expression in the development of lymph node metastasis in gastric cancer. *Clin Cancer Res* **5**(7): 1823–1829.

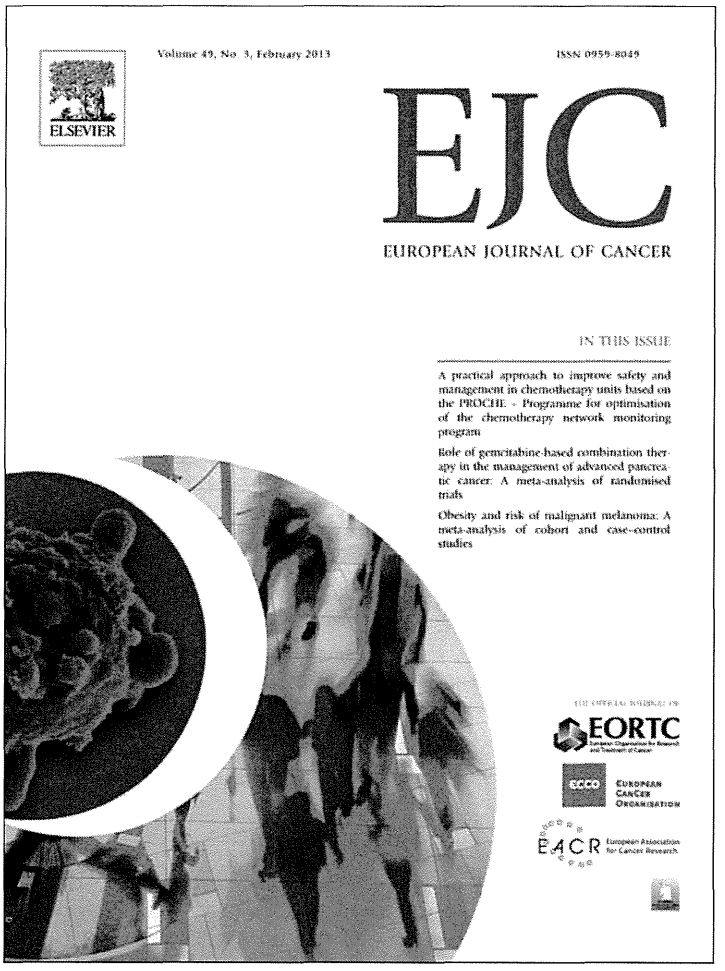

European Journal of Cancer (2013) 49, 741–751

Available at www.sciencedirect.com

SciVerse ScienceDirect

journal homepage: www.ejcancer.info

High mobility group box 1 released from necrotic cells enhances regrowth and metastasis of cancer cells that have survived chemotherapy

Yi Luo [a], Yoshitomo Chihara [a,b], Kiyohide Fujimoto [b], Tomonori Sasahira [a], Masaomi Kuwada [b], Rina Fujiwara [a], Kiyomu Fujii [a], Hitoshi Ohmori [a], Hiroki Kuniyasu [a,*]

[a] *Department of Molecular Pathology, Nara Medical University, Kashihara, Japan*
[b] *Department of Urology, Nara Medical University, Kashihara, Japan*

Available online 3 October 2012

KEYWORDS
HMGB1
Necrosis
Apoptosis
TLR4
RAGE

Abstract The role of the high mobility group box 1 (HMGB1) protein in chemotherapy-induced cell death was examined. CT26 mouse colon cancer cells were treated with trichostatin A (TSA; apoptosis inducer) or doxorubicin (DXR; necrosis inducer). DXR increased HMGB1 concentration in CT26 cell culture medium, whereas TSA did not. In a CT26 bilateral subcutaneous tumour model, DXR or TSA was injected in a single tumour. After injection, serum HMGB1 concentration in DXR-treated mice was 10 times higher than that in TSA-treated mice. After DXR treatment, the contralateral and remnant tumours showed more pronounced growth than did those treated with TSA. In mouse models, lung and liver metastasis was enhanced by DXR but not by TSA. DXR-enhanced metastasis was abrogated by anti-HMGB1 antibody treatment. In a cancer dormancy model, DXR induced regrowth of quiescent CT26 cells. HMGB1 induced tumour necrosis factor-α secretion via Toll-like receptor (TLR)4 in U937 monocytes; however, HMGB1 decreased the number of U937 cells, resulting in restriction of immune activation via receptor for advanced glycation endproducts (RAGE). RAGE showed a more pronounced effect on nuclear factor kappa B activation than did TLR4 in CT26 cells. These findings suggest that HMGB1 released from necrotic cancer cells treated with a necrosis inducer enhances regrowth and metastasis of remnant cancer cells via RAGE activation.

1. Introduction

Cancer chemotherapy aims to reduce the number of cancer cells by induction of cell death. Indeed, necrosis

* *Corresponding author:* Address: Department of Molecular Pathology, Nara Medical University, 840 Shijo-cho, Kashihara, Nara 634-8521, Japan. Tel.: +81 744 22 3051; fax: +81 744 25 7308.
E-mail address: cooninh@zb4.so-net.ne.jp (H. Kuniyasu).

0959-8049/$ - see front matter © 2012 Elsevier Ltd. All rights reserved.
http://dx.doi.org/10.1016/j.ejca.2012.09.016

is a common reaction of cancer cells to anti-cancer drugs. High mobility group box 1 (HMGB1) is a cancer progression-related protein and has been shown to be released from necrotic cells.[1,2] Thus, in view of the massive cell necrosis caused by cancer chemotherapy, the role of HMGB1 in chemotherapy needed to be examined.

The HMGB1 protein is a non-histone chromosomal protein found in eukaryotic cells.[3–5] It is a multifunctional protein that has diverse biological functions in both normal and cancer cells. For instance, HMGB1 possesses DNA-binding properties that permit HMGB1 to regulate multiple processes, including transcription, replication, recombination, DNA repair, genomic stability and activation of Toll-like receptor (TLR)4.[6,7] Furthermore, HMGB1 is associated with cell motility, as observed in neuritis outgrowth,[4] and also with cancer cell invasion.[8] HMGB1 is secreted from activated monocytes, macrophages and natural killer cells, and acts extracellularly as a proinflammatory cytokine.[9,10] Cancer cells also secrete and overexpress HMGB1 by stimulation of growth factors, cytokines and cellular stresses that involve advanced glycation endproducts (AGE) and deoxycholic acid.[11–14] Secreted HMGB1 acts as a ligand to activate the receptor for advanced glycation endproducts (RAGE), thereby inducing cell growth, motility, invasion, angiogenesis and metastasis.[8,12,15–18]

HMGB1 is released from cells by both active and passive processes. Active secretion of HMGB1 is associated with detachment from loosened chromosomes by histone acetylation, HMGB1 hyperacetylation and monomethylation of HMGB1 at Lys42.[14,19,20] The mechanism of cytoplasmic HMGB1 secretion from human monocytes is associated with an atypical endolysosomal-like secretory pathway.[21] In contrast, HMGB1 is released from necrotic cells by passive diffusion.[2] However, HMGB1 is not released from the tightly-packed nuclei of apoptotic cells and triggers inflammation.

HMGB1 is an agonist of RAGE and TLR4; however, both receptors are expressed on cancer cells and immune cells.[22,23] In the present study, we compared the effects of HMGB1 on cancer cell regrowth and metastasis after treatment with necrotic anti-cancer drugs or apoptosis-inducers.

2. Materials and methods

2.1. Cell culture and reagents

CT26 mouse colon cancer cell line was kindly provided from Professor Isaiah J. Fidler (M.D. Anderson Cancer Center, USA).[24] LL2 murine lung cancer cell line and HT29 human colon cancer cell line were purchased (Dainihon Pharmaceutical, Tokyo, Japan). Cells were maintained in Dulbecco's modified essential medium (Sigma Chemical Co., St. Louis, USA) containing 10% foetal bovine serum (Sigma) under the conditions of 5% CO_2 in air at 37 °C. Sodium nitroprusside (SNP; Sigma), trichostatin A (TSA; Wako Pure Chemical, Osaka, Japan), linoleic acid (LA; Sigma), doxorubicin (DXR; Sigma), ethyl pyruvate (EP; Wako), human recombinant HMGB1 and anti-HMGB1 antibody (R&D Systems, Minneapolis, USA) were purchased.

2.2. Assessment of cell growth and apoptosis

Cells growth was assessed by MTT assay according to the previous description.[23] Apoptosis and necrosis were assessed by apoptosis/necrosis detection kit (Enzo Life Sciences, Plymouth Meeting, USA). In the kit, apoptotic and necrotic cells were labelled fluorescently by annexin V-EnzoGold and 7-AAD, respectively. Cells (2000) were observed to determine apoptosis or necrosis under fluorescent microscope. The experiments were performed in triplicate. Lactate dehydrogenase C (LDH) and Terminal deoxynucleotidyl transferase (TdT)-mediated dUTP-biotin nick end labelling (TUNEL) were also examined. Colony formation assay in soft agar gel was performed according to our previous report.[25]

2.3. Cultured medium

CT26 cells (1×10^8) were cultured with regular medium containing 50% inhibitory concentration (IC50) concentration of DXR (0.5 μg/ml) and TSA (62 μg/ml), or PBS for the control for 24 h. The cultured media were collected and filtrated with 0.2 μm filter (Becton-Dickinson Labware, Bedford, USA). CT26 cells were treated with the mixture of fresh regular medium and the cultured medium for 24 h and the living cell number was counted by Autocytometer (Sysmecs, Kobe, Japan).

2.4. Animal model

BALB/c, C57BL6 and athymic nu nu BALB/c mice (male, 4 weeks old), purchased from Japan SLC (Shizuoka, Japan), were maintained according to the institutional guidelines approved by the Committee for Animal Experimentation of Nara Medical University. Single-cell suspensions of CT26 cells (1×10^7) in Hanks solution were injected into the scapular regions of mice at day 1. In the bilateral tumour model, CT26 cells (1×10^7) were injected into the bilateral scapular regions of mice. For a rapid growth model, cell (1×10^8) were inoculated. For metastasis model, CT26 cells (1×10^6) were injected into the spleen and the tail vein to form metastasis in the liver and lung, respectively, at day 6. DXR or TSA were injected into the back tumour at day 8. Serum HMGB1 was examined ay day 9. Anti-HMGB1 antibody (R&D, 5 and 20 μg in 200 μl PBS for 10^7 and 10^8 cells inoculated, respectively) was administrated intraperitoneally at defined date. The dosage

was calculated for neutralising 2 or 8 μg/ml of HMGB1 in a 20-g weight mouse.[26] EP (30 mg/kg body weight) was administrated intraperitoneally. The tumour volume was calculated by a formula of (short diameter/2)^2 × long diameter × π.

2.5. Dormancy model

CT26 cells were treated with LA (200 μg/ml) for 6 weeks, which induced quiescence to the cells. The quiescent CT26 cells (1×10^6) were inoculated in the contralateral side of the back at day 6.[13]

2.6. TUNEL assay

TUNEL assay using the *In Situ* Cell Death Detection Kit, POD (Roche Diagnostics, Indianapolis, USA). The percent frequency of TUNEL-positive cells was calculated from the ratio of positive nuclei to 500 examined nuclei.

2.7. Enzyme-linked immunosorbent assay (ELISA)

Mouse blood was collected from the heart or caudal vein. The blood was rapidly centrifuged by 500*g*, 4 min at 4 °C. The supernatant was used as serum. Cultured medium (200 μl) filtrated with 0.2 μm filter (Becton-Dickinson) was used for ELISA. HMGB1, LDH and TNF-α in serum or cultured medium were measured by each specific ELISA kit (Shinotest, Tokyo, Japan, Uscn Life Science, Uhan, China, and Abnova, Taipei City, Taiwan, respectively). ELISA was performed according to provider's instructions. The experiment was repeated three times.

2.8. Small interfering RNA (siRNA)

Stealth Select RNAi for RAGE, and TLR4 were purchased from Invitrogen (Carlsbad, USA). AllStars siRNA was used for control (Qiagen). siRNA (20 nM) was transfected with Lipofectamine 2000 (Invitrogen) according to the provider's instructions.

2.9. Quantitative reverse transcription-polymerase chain reaction (RT-PCR)

Total RNA was extracted using RNeasy Mini Kit (Qiagen) and total RNA (1 μg) was synthesised with the ReverTra Ace qRT Kit (Toyobo, Osaka, Japan). Quantitative reverse transcription-polymerase chain reaction was performed on StepOne Plus Real-Time PCR Systems (Applied Biosystems, Foster City, USA) using TaqMan Fast Universal PCR Master Mix (Applied Biosystems) and analyse the relative standard curve quantification method. PCR condition was according to the manufacturer's instructions and ACTB mRNA level was amplified for internal control. TaqMan Gene Expression Assays of RAGE, TLR4 and ACTB were purchased from Applied Biosystems. All PCRs were done at triplicate.

2.10. Immunoblot analysis

Whole-cell lysates were prepared as described previously.[23] Nuclear fraction was extracted as described previously.[14] Fifty-microgram lysates were subjected to immunoblot analysis in 12.5% sodium dodecyl sulphate–polyacrylamide gels followed by electrotransfer (SDS–PAGE) to nitrocellulose filters. For examining oxidised HMGB1, the lysates were separated in a non-reduced condition by SDS–PAGE.[26] The immune complex was visualised with an ECL system (Amersham, Aylesbury, UK). Antibodies to nuclear factor kappa B (NFκB) p65, IκB, extracellular signal-regulated protein kinase (ERK)1/2, and phosphorylated ERK1/2 (Santa-Cruz Biotechnology, Santa Cruz, USA), HMGB1 (R&D Systems), and microtubule-associated protein light chain (LC)3 (CosmoBio, Tokyo, Japan) were used for primary reaction.

2.11. Statistical analysis

Statistical analyses of experimental data were performed using Mann–Whitney *U* test, Kruskal–Wallis test with Dunn's multiple comparison test (non-parametric ANOVA). Statistical significance was defined as a two-sided *P* value of less than 0.05.

3. Results

3.1. Effect of cell death inducers on CT26 cell growth

First, we examined the effect of four cell death inducers, SNP, TSA, LA and DXR, on the growth of CT26 mouse colon cancer cells (Fig. 1). Treatment with cell death inducers resulted in a dose-dependent decrease in CT26 cell numbers (Fig. 1a–d). A longer treatment showed that the apoptosis-inducers continued to induce cell decrease, whereas the effect of the necrosis-inducers was close to a plateau (Fig. 1e). A colony formation assay showed that the necrosis-inducers increased the colony number at week 4 in comparison with those at week 2 (Fig. 1f). The induction of apoptosis or necrosis was quantified at the IC50 of cell death inducers (Fig. 1g). LA and DXR induced mainly necrosis, whereas SNP and TSA induced mainly apoptosis. The induction of necrosis and apoptosis were confirmed by LDH release and TUNEL, respectively (Fig. 1h).

3.2. Secondary effect of cell death on remnant cells

To examine the effect of induction of cell death on remnant living cells, we cultured CT26 cells in a medium supplemented with DXR and TSA of the concentrations at